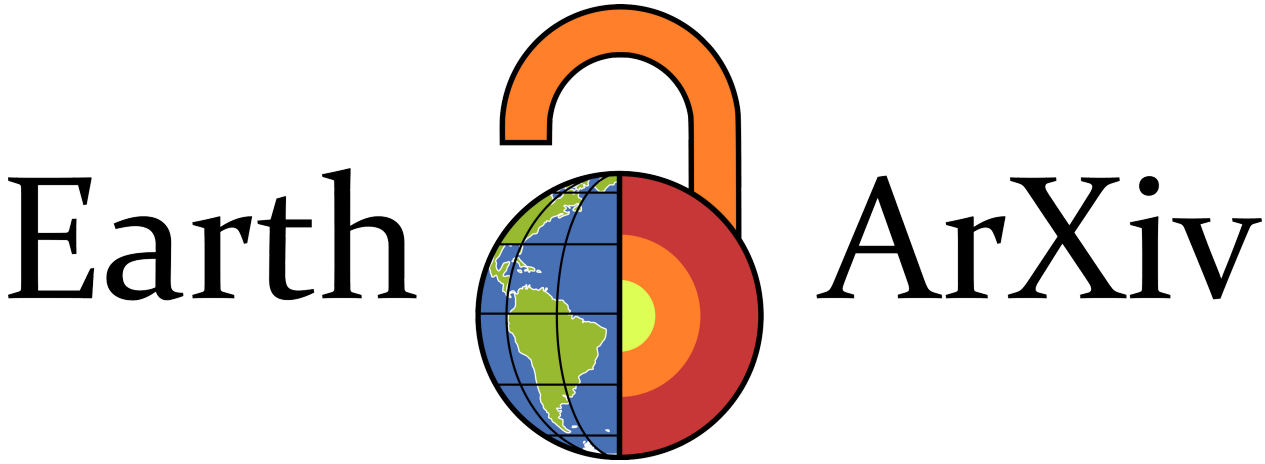

This manuscript has been submitted for publication in *Science of the Total Environment*. Please note the manuscript has yet to be formally accepted for publication. Subsequent versions of this manuscript may have slightly different content. If accepted, the final version of this manuscript will be available via the 'Peer-reviewed Publication DOI' link on the right-hand side of this webpage. Please feel free to contact any of the authors; we welcome feedback.

Long-term trends and drivers of water color in Missouri reservoirs

Lorena Pinheiro-Silva[1,2*], Greg M. Silsbe[1], David C. Richardson[2,3], Rebecca L. North[2]

[1]Horn Point Laboratory, University of Maryland Center for Environmental Science, Cambridge, Maryland, USA.

[2]School of Natural Resources, University of Missouri-Columbia, Columbia, Missouri, USA.

[3]State University of New York at New Paltz, New Paltz, New York, USA.

* corresponding author: lsilva@umces.edu

Abstract

Contrasting water quality trends are occurring within and across North America, with waterbodies experiencing increasing phytoplankton blooms, increasing dissolved organic matter, or both. Simultaneously, other waterbodies are becoming clearer and bluer; dramatically changing water color. To assess the spatial and temporal variability in water color, we quantified trends in satellite-derived dominant wavelength (λ_d) from 1984 to 2020 from the LimnoSat-US for 478 reservoirs in Missouri, USA. We also analyzed trends in summer water quality (WQ) parameters from two long-term monitoring programs to compare with observed water color changes. We demonstrate that λ_d is a robust indicator of water quality, including nutrients (total nitrogen and total phosphorus) that are not typically associated with satellite-derived data. Currently, the vast majority of Missouri reservoirs (94%) are classified as green and within a range (538−555 nm) that lies closer to the brown, rather than blue, color endmember. Nearly one-third of reservoirs (n = 155) experienced significant temporal shifts in water color, with more (n = 92) negative (e.g., bluer) than positive (n = 63) λ_d trends; although shifts were largely confined to the green region of the visible spectrum. This result agrees with observed WQ trends within individual reservoirs that show indices of eutrophication and nutrient reductions. Linear mixed-effect models indicate that periods of extreme wetness and drought are associated with browner and bluer waters, respectively, and boosted regression trees further reveal that waterbody and watershed characteristics are important predictors for water color trends. Our results help explain some of the previously observed heterogeneous controls on water color and emphasize the importance of integrating water quality data alongside commonly used landscape and morphological features. This is important not only to better understand regional trends in water color, but also to link these trends to changes in watershed characteristics and their impact on waterbody-specific processes.

Keywords: Midwest reservoirs, dominant wavelength, water quality, satellite remote sensing.

1. Introduction

Contrasting water quality trends are occurring within and across North America, with lakes experiencing eutrophication (aka 'greening'; Schindler et al., 2012), brownification (aka 'browning'; Monteith et al., 2007; Roulet and Moore, 2006), or both simultaneously (aka "murky" lakes; Leech et al., 2018), while others are undergoing oligotrophication (aka 'blueing'; Sillen et al., 2024). Water color, as perceived by the human eye, is one of the oldest indicators of water quality and is closely linked to productivity and trophic state of aquatic ecosystems (Topp et al., 2021). For instance, high nutrient loads into waterbodies from urban, agricultural, and industrial sources result in increased phytoplankton biomass and greener waters (Dodds et al., 2009). Increases in colored dissolved organic matter (CDOM) due to changes in climate, hydrology, land cover, and atmospheric deposition (Erlandsson et al., 2008; Freeman et al., 2001; Monteith et al., 2007) have led to brown waters (Leech et al., 2018). Conversely, factors such as lake acidification (Charifson et al., 2015), low precipitation (Hongve et al., 2004), increased rates of filter-feeding by zebra mussels (Binding et al., 2007), or reductions in nutrient loading (Jeppesen et al., 2005) lead to increased water transparency and bluer waters. The nutrient-color paradigm (Williamson et al., 1999) conceptualizes the interaction between total phosphorus (TP) and CDOM in lakes where blue waters are oligotrophic (low TP and CDOM), green waters are eutrophic (high TP, low CDOM), and brown waters are either dystrophic (low TP, high CDOM) or mixotrophic ('murky', high TP and CDOM; Oleksy et al., 2024; Williamson et al., 1999). Water color's strong representativeness and accessibility through remote sensing make it an effective indicator for monitoring changes in the ecological state and environmental conditions of aquatic ecosystems (Shen et al., 2025), helping to reveal the impacts of global environmental changes (e.g., climate, land use).

Changes in precipitation and evapotranspiration patterns in response to climate change, including severe sustained weather like droughts or flooding, can also significantly alter water quality (Woolway et al., 2020). Similar to other parts of the world, reservoirs across the Midwestern USA are experiencing intensifying

hydroclimatic extremes as a result of climate change. For instance, climate projections indicate an increased likelihood of drought events in this region, both in terms of in frequency and magnitude (Strzepek et al., 2010). In Missouri reservoirs, a previous study showed that during dry years when Secchi depths are deeper, particulate organic matter (POM) and chlorophyll *a* are strongly correlated (Bhattacharya et al., 2022), reflecting increased phytoplankton production. Under these conditions, these reservoirs are likely to experience 'greening' (Bhattacharya et al., 2022), in contrast to reservoirs in other regions facing wetter conditions, where increased runoff drives 'browning' due to higher terrestrial organic matter inputs (Roulet and Moore, 2006).

The scarcity of long-term *in-situ* data across broad spatial scales has limited our ability to detect and understand water quality trends at regional and continental scales. Satellite-based monitoring offers a cost-effective alternative, providing high spatial and temporal resolution to assess waterbodies experiencing significant environmental changes. Remote sensing has been widely used to monitor optically active parameters such as chlorophyll *a* (Smith et al., 2020) and other accessory pigments (McKibben et al., 2024), water clarity (Secchi disk; Binding et al., 2007), turbidity (Dogliotti et al., 2015), suspended sediments (Ondrusek et al., 2012), colored dissolved organic matter and dissolved organic carbon (Cao et al., 2018), as well as non-optically active compounds such as total phosphorus (Xiong et al., 2022) and total nitrogen (Li et al., 2022). However, progress in the remote sensing of inland waters has been hindered by the limited capabilities of satellite sensors (e.g., spectral, spatial, and temporal coverage) not originally designed for coastal and inland waters applications (Mouw et al., 2015). Additionally, challenges such as complex atmospheric correction due to absorbing aerosols (e.g., smoke, dust, and anthropogenic emissions like CO_2), land adjacency effects, and bottom reflectance, further complicate the accuracy of water quality parameter retrievals in inland water ecosystems (Mouw et al., 2015). However, continued improvements in atmospheric correction algorithms (Vanhellemont, 2019), machine learning approaches (Smith et al., 2020), and the creation of robust analysis-ready databases (Topp et al., 2020) collectively aim to improve data quality and accessibility.

This study aims to understand the extent, magnitude, and underlying factors driving shifts in water color in Missouri reservoirs. We used 37 years of satellite-derived water color data along with detailed field-based water quality measurements to (1) quantify how summer water color and water quality parameters have changed over the last three decades, and (2) identify climate, catchment, and waterbody factors driving the observed spatial and temporal trends in water color. With particulate organic matter (POM) concentrations reported to typically dominate summer seston in Missouri reservoirs (Petty et al., 2020), we predict that the abundance of 'green' waterbodies will increase while 'brown' waterbodies will decrease. Based on this prediction, we expect an overall trend toward decreasing dominant wavelength (λ_d) over time. By compiling a uniform dataset from open data repositories and two statewide long-term water quality monitoring programs, our study not only aims to unravel the key drivers of regional trends in water color in the study region, but also demonstrates the potential for integrating satellite-based measurements with traditional monitoring to strengthen future research; particularly in times of reduced funding for environmental monitoring programs.

2. Material and Methods

2.1 Study Area and Geospatial Analysis

Most of Missouri's (MO) waterbodies are human-constructed reservoirs embedded across the state's six Environmental Protection Agency (EPA) ecoregions (Ozark Highlands, Central Irregular Plains, Western Corn Belt Plains, Interior River Valleys and Hills, the Mississippi Alluvial Plain, and Mississippi Valley Loess Plains; Fig. 1a). Geospatial data for individual reservoirs, published by the MO Department of Natural Resources (MDNR) was separately matched in space with the *in situ* water quality monitoring datasets and the remote sensing dataset described below. The MDNR identifies a total of 2,547 reservoirs, of which 478 have remotely sensed data with ≥ 20 consecutive years of summer color observations (Section 2.2); 298 have water quality data (Section 2.3), and 135 have co-located water quality and remotely sensed time series (Fig. 1a).

Watersheds were delineated using the Python package PySheds (software references listed in Supplementary Material; Table S1) and USGS 60 m digital elevation data. Watershed land cover was extracted from the 2021 release of the National Land Cover Database (NLCD), developed primarily by the U.S. Geological Survey (USGS) in collaboration with the Multi-Resolution Land Characteristics (MRLC) Consortium, at a 30-meter spatial resolution. Amongst the reservoirs with remotely sensed time series (n = 478), watersheds were classified as 'agriculture' (n = 218, pasture and crops), 'forest' (n = 141, deciduous, evergreen, mixed), 'urban' (n = 22, low, medium, and high intensity development), 'open water' (n = 1, when the reservoir accounts for most of the watershed), and 'wetland' (n = 11), when land cover of a single type exceeded 50% of the watershed (Fig. 1b). Watersheds with no predominant land cover (< 50%) were identified as "mixed" watersheds (n = 85).

Geomorphological data were derived for each reservoir and its associated watershed. Elevation, area, perimeter, and elongation ratios were calculated. The elongation ratio is defined as the ratio of the diameter of a circle with an equivalent area to that of the reservoir/watershed to its maximum length (i.e., the maximum distance between all coordinate pairs along the perimeter; Sukristiyanti et al., 2018). Thus, high elongation ratios are more circular reservoirs/watersheds that generally coincide with flat land and low relief; whereas, smaller elongation ratios correspond to narrow and dendritic waterbodies with high relief and steep slopes (Sukristiyanti et al., 2018). All geospatial analysis was performed in Python, and the functions and libraries used for each calculation are listed in the Supplementary Material (Table S1).

Hydrometeorological variations in space and time were analyzed using the Palmer drought severity index (PDSI). The PDSI index quantifies the severity of wet and dry conditions by using estimates of relative soil moisture conditions based on temperature, precipitation, and evapotranspiration anomalies. PDSI values less than -3 indicate severe drought conditions, and PDSI values greater than 3 indicate very moist conditions. PDSI for summers from 1990 to 2020 were obtained from the daily high-spatial resolution Gridded Surface

Meteorological (gridMET) dataset available on the Google Earth Engine (GEE) platform by the title GRIDMET DROUGHT:CONUS DROUGHT Indices.

2.2 Water Color

Remotely-sensed reflectance data and the resultant visible dominant wavelength (λ_d) were tabulated for 478 waterbodies in Missouri from the LimnoSat-US database (Topp et al., 2020). The main criterion for selecting the studied reservoirs was the availability of 20 consecutive years of data between 1984 and 2020. For inland waterbodies in the U.S. larger than 0.1 km^2, LimnoSat contains all cloud-free Landsat (5, 7, and 8) surface reflectance (T1-SR) data where for each waterbody and timestamp, the median reflectance is derived from pixels within 120 m of the Chebyshev Center (i.e., the deepest point that is furthest away from the shoreline). Landsat 5 and Landsat 7 imagery have been atmospherically corrected using the Landsat Ecosystem Disturbance Adaptive Processing System (LEDAPS), while Landsat 8 imagery has been corrected using the Landsat Surface Reflectance Code (LaSRC). Bands for each sensor were standardized across time and between satellites (Topp et al., 2021), ensuring the reliability of long-term trend analyses (Shen et al., 2025). Dominant wavelength is calculated by converting surface reflectance values into the chromaticity color space, following Wang et al. (2015). First, tristimulus values (X, Y, Z; Eqn. 1) are derived from surface reflectance in red, green, and blue bands.

$$X = K\int_{380}^{700} S(\lambda).\rho(\lambda).\bar{x}(\lambda)d\lambda = K\int_{380}^{700} \phi(\lambda).\bar{x}\,(\lambda)d\lambda$$

$$Y = K\int_{380}^{700} S(\lambda).\rho(\lambda).\bar{y}(\lambda)d\lambda = K\int_{380}^{700} \phi(\lambda).\bar{y}\,(\lambda)d\lambda$$

$$Z = K\int_{380}^{700} S(\lambda).\rho(\lambda).\bar{z}(\lambda)d\lambda = K\int_{380}^{700} \phi(\lambda).\bar{z}\,(\lambda)d\lambda \quad (1)$$

Where $\bar{x}(\lambda)$, $\bar{y}(\lambda)$, and $\bar{z}(\lambda)$ are the color-mixture values for equal energy spectrums obtained using the lookup table provided by the International Commission on Illumination (CIE).

These tristimulus values are then used to compute the chromaticity coordinates (x, y, z; Eqn. 2), which are subsequently transformed into a new coordinate system (x', y'; Eqn. 3).

$$x = \frac{X}{X+Y+Z}$$

$$y = \frac{Y}{X+Y+Z}$$

$$z = \frac{Z}{X+Y+Z} \quad (2)$$

$$x' = y - 0.3333$$

$$y' = x - 0.3333 \quad (3)$$

Since x + y + z = 1, the hue angle is calculated using two transformed chromaticity coordinates (x', y'; see Wang et al., 2015) and then geometrically mapped to a λ_d based on its position within the two-dimensional CIE chromaticity diagram. The hue angle represents the pure color that most closely resembles the observed color of natural waters. For each reservoir and year, the mean λ_d was computed across the stratified season (May 1 to Oct 31) to align with the water quality sampling period. The representation of λ_d as color in figures presented below was derived by taking the median red, green, and blue remote-sensing reflectance values across all LimnoSat data in the study area. These data were used to delineate broad water color groups defined as blue ($\lambda_d \leq 495$ nm), green (495 nm $< \lambda_d <$ 575 nm), and brown ($\lambda_d \geq 575$ nm). Within the green spectral range, blue reflectance steadily declines while red reflectance steadily increases (Fig. S1), such that decreasing trends in λ_d can be ascribed as blueing and increasing trends in λ_d can be described as browning.

2.3 In situ water quality dataset

Water quality parameters for 298 waterbodies in Missouri from 1984 to 2020 were obtained through the Statewide Lake Assessment Program (SLAP) and the community science led Lakes of Missouri Volunteer Program (LMVP), aligning with the LimnoSat-US data availability. Collectively, these two long-term water

171 quality monitoring programs record measurements of total nitrogen, total phosphorus, chlorophyll *a*, Secchi
172 disk depth, particulate organic and inorganic matter, as well as profile data (temperature, depth, and oxygen) on
173 reservoirs across the state every year. In each waterbody, surface water samples are collected on 3 or 4
174 occasions between May and October each year, in close proximity to the deepest part of the reservoir (i.e., near-
175 dam locations). When surface samples were not available, epilimnetic integrated samples were used instead
176 (Fig. S2).

177 Surface water temperature (wtemp; ℃) was measured within 0.5 m of the water surface in each
178 reservoir. Water temperature and dissolved oxygen profiles, recorded in meter increments (1984 – 2016) or
179 continuous profiles (2017 – 2020) from the surface to the bottom, were obtained using multiple YSI sondes over
180 the years (see Table S2). These data were used to calculate average water temperature and dissolved oxygen
181 concentrations in the epilimnion (above the top of the metalimnion) and the hypolimnion (below the bottom of
182 the metalimnion). The thermal stability index, Brunt-Väisälä buoyancy frequency (N^2; s^{-2}), was calculated based
183 on the density gradient of the water column in the R statistical environment, version 4.4.2 (The R Development
184 Core Team 2024; Table S1). Thermocline depth at 0.3 kg m^{-3}/m density threshold was derived from water
185 temperature profiles. Water transparency (Secchi) was assessed using a Secchi disk. Water samples were stored
186 in high density polyethylene (HDPE) bottles, placed into coolers, and processed within 12-h of collection. After
187 freezing, they were analyzed by standard methods (Table S2) for particulate organic matter (POM; mg/L),
188 particulate inorganic matter (PIM; mg/L), total suspended solids (TSS; mg/L), total phosphorus (TP; µmol/L),
189 total nitrogen (TN; µmol/L), uncorrected chlorophyll *a* (Chl *a*; µg/L), and dissolved organic carbon (DOC;
190 µmol/L). Sampling and analytical methodology were consistent throughout, except for chl *a*, TP, and TN (Table
191 S2). We also determined the ratios of TN and TP (TN/TP), POM and TSS (POM/TSS), PIM and TSS
192 (PIM/TSS).
193

194 *2.4 Data Analysis*

195 *2.4.1 Linear mixed-effects models*

196 To quantify the influence of climatic variability (e.g., drought and wetter climate) on water color (λ_d), we
197 employed linear mixed-effect models (LMMs; Fig. 2; see Table S3 for statistical references). In all models, λ_d
198 was the response variable, with reservoir identity included as a random intercept to account for inter-reservoir
199 variability in water color. Fixed effects included PDSI, ecoregion, and their interaction. The inclusion of the
200 interaction term allows us to account for climatic effects that might differ by ecoregion. To capture possible
201 underlying temporal trends in λ_d across reservoirs, year was included as a numeric covariate. The variance
202 explained by LMMs was based on marginal and conditional adjusted R^2 (Nakagawa and Schielzeth, 2013).
203 Marginal adjusted R^2 (R^2m) represents the variance explained by a fixed term, and conditional R^2 (R^2c)
204 represents the variance explained by both fixed and random terms. A visual examination of diagnostic plots was
205 applied to determine the model's goodness of fit. *p*-values and 95% confidence intervals were calculated using
206 Wald t-tests with Satterthwaite's approximation of degrees of freedom. All models were implemented in the R
207 statistical environment, version 4.4.2 (The R Development Core Team 2024). The functions and libraries used
208 are listed in the Supplementary Material (Table S1).
209
210 *2.4.2 Remotely sensed and in situ water quality matchup analysis*
211 Discrete water quality data were co-located in space and time with satellite-derived water color data using a 1-
212 day time window from satellite overpass, resulting in 1701 matchups (Fig. 2). The final dataset includes λ_d
213 values paired with near-concurrent *in situ* measurements of Chl *a*, Secchi disk depth, TN, TP, PIM, POM, and
214 DOC across multiple reservoirs. To assess differences across wavelengths, water quality data were grouped by
215 λ_d values binned every 10 nm and tested for statistically significant differences using nonparametric Kruskal-
216 Wallis tests. When significant differences were detected, pairwise Dunn's post-hoc tests with Bonferroni-

adjusted *p*-values were applied to evaluate differences in each variable between λ_d bins. Lastly, Spearman pairwise rank correlations were used to evaluate associations between water quality parameters and λ_d values.

2.4.3 Trend analysis

To evaluate the annual rate of change in water color ($\Delta\lambda_d$), both overall and reservoir-specific trends in λ_d from 1984 to 2020 were estimated using Sen's slope (*Q*; see Table S3 for statistical references), and the statistical significance of resultant trends was assessed using the non-parametric Mann-Kendall trend test (*MK*; see Table S3 for statistical references). For the overall trend, summer annual mean λ_d values were calculated across all reservoirs (Fig. 2). For reservoir-specific trends, summer annual mean λ_d values were calculated individually for each reservoir. To ensure reliable trend estimates, our analysis includes only reservoirs with a minimum of 20 consecutive years of data between 1984 and 2020 (*n* = 478, Fig. S3). Missing values in the time series were imputed using linear interpolation, allowing a maximum gap of two consecutive missing years. Missing values at the beginning or end of the time series were not interpolated. Statistically significant ($p \leq 0.05$) trends in λ_d were categorized based on the direction of change according to the *Q* value. An increasing trend in λ_d (positive *Q* value) represents a shift toward longer λ_d (i.e., greener or browner waters), while a decreasing trend (negative *Q* value) indicates a shift toward shorter λ_d (i.e., greener or bluer waters). To assess differences in the most recent λ_d and $\Delta\lambda_d$ across ecoregions and watershed land cover types, we used nonparametric Kruskal-Wallis tests. When significant differences were found, pairwise Dunn's post-hoc tests with Bonferroni-adjusted *p*-values were applied to identify specific group differences.

To quantify the trends in summer mean water quality parameters, we employed the same statistical approach described above. Statistically significant ($p \leq 0.05$) interannual trends were categorized based on the direction of change (i.e., increasing or decreasing) using the *Q* value. Trend analysis was restricted to reservoirs with at least 10 consecutive years of data between 1984 and 2020 (Fig. 2). Not all reservoirs (*n* = 298) have the

required time series available for every variable (Fig. S3). The total number of reservoirs analyzed for each physical and chemical water quality variable was as follows: Chl *a*, Secchi, TN, TP, TN/TP (n = 130), PIM, POM, TSS, POM/TSS, PIM/TSS (n = 127), wtemp, hypolimnion wtemp, thermal stability (n = 83), thermocline (n = 82), dissolved oxygen profile metrics (n = 62–70), and DOC (n = 45). Lastly, Spearman pairwise rank correlations were used to assess the strength and direction of associations between long-term trends (i.e., slopes) of water quality parameters. Trend analysis was performed in the R statistical environment, version 4.4.2 (The R Development Core Team 2024). The functions and libraries used are listed in the Supplementary Material (Table S1).

2.4.4 Boosted Regression Trees (BRTs)

To quantify the relative contribution of reservoir catchment characteristics, morphology, and limnological parameters to the dominant wavelength slope ($\Delta\lambda_d$), we employed Boosted Regression Trees (BRTs). For each reservoir, we first calculated the average value of each predictor variable across the available temporal records, requiring a minimum of five years of data to be included in the analysis (Fig. 2). These reservoir-level means were then used in the BRTs to identify the most influential predictors of $\Delta\lambda_d$. Our final dataset included 135 reservoirs with co-located LimnoSat and *in situ* water quality data, sampled between 1984 and 2020. The BRT method is a machine learning technique that combines regression decision trees and a boosting algorithm (Elith et al., 2008). At each step, a new tree that best reduces the loss function is fitted to the residuals without changing the existing trees as the model is enlarged (i.e., stagewise). This approach eliminates the need for prior data transformation or outlier elimination, fits complex nonlinear relationships between explanatory and response variables, handles interaction effects between predictors, and accommodates both categorical and numeric variables, as well as missing data (Elith et al., 2008). BRTs were implemented in the R statistical environment, version 4.4.2 (The R Development Core Team 2024) using the *gbm.step* function, which

incorporates cross-validation to identify the optimal number of trees and implements the procedures described by Elith et al. (2008). The functions and libraries used are listed in the Supplementary Material (Table S1).

In BRT modelling, three hyperparameters need to be defined and tuned: The learning rate (*lr*), which determines the contribution of each tree to the final fitted model; tree complexity (*tc*), which controls the size of trees and whether interactions between variables should be considered; bag fraction (*bf*), which specifies the proportion of data, without replacement, from the full training set to be selected at each step. The number of trees (*nt*) is determined from the combination of *lr* and *tc* and, in practice, smaller learning rates and larger tree complexities increase the number of trees. To select the appropriate structure of the BRTs, we fitted 30 combinations with varying values for *lr* (0.05, 0.01, 0.005, 0.001, 0.0005), *tc* (1, 5, 10) and *bf* (0.5, 0.75). Model potential for overfitting and performance was assessed using an 80:20 train:test data split with a 10-fold cross-validation method. First, models with the lowest prediction deviation (i.e., deviance between observed values from the training set and predicted values from the test set) were selected. Then, the performance of these models was further evaluated using three metrics: mean absolute error (MAE; Eq. 4), root mean square difference (RMSE; Eq. 5), and coefficient of determination (R^2; Eq. 6). Final model selection was based on the combination of lowest MAE and RMSE and highest R^2 value (i.e., higher R^2 reflects better predictive performance). The metrics were calculated as follows:

$$MAE = \frac{1}{n}\sum_{i=1}^{n}|P_i - O_i| \quad (4)$$

$$RMSE = \sqrt{\frac{1}{n}\sum_{i=1}^{n}(P_i - O_i)^2} \quad (5)$$

$$R^2 = \frac{\sum_{i=1}^{n}(P_i - \bar{O})^2}{\sum_{i=1}^{n}(O_i - \bar{O})^2} \quad (6)$$

Where n is the number of observations, P_i and O_i are the predicted and observed values at i, respectively, and $\bar{O}$ is the mean of the observed data. MAE indicates how close the prediction is to the observed values, while

RMSE represents the standard deviation of the residuals. R^2 represents the predictive accuracy of models; it approaches 1 when prediction becomes optimal.

The final optimal values of *lr*, *tc*, and *bf* were set to 0.0005, 5, and 0.75, respectively, with a maximum number of trees = 3,200 and a Gaussian error distribution (Table S4). The selected model was used to calculate the mean relative importance (RI) and cumulative contribution of each predictor in explaining the variability of $\Delta\lambda_d$. The RI is quantified by analyzing the number of times a predictor is selected for splits in regression trees and the improvement it brings to the model's predictive accuracy. The RI of each variable is given by dividing its importance by the sum of importance values across all explanatory variables, collectively summing to 100% (Elith et al., 2008). Higher RI values indicate a stronger influence on the response variable. The cumulative contribution reflects the combined effect of multiple predictors in explaining $\Delta\lambda_d$. It is calculated by ranking predictors in descending order of their mean RI and computing their cumulative contributions as a percentage of the total importance. Significant predictors based on permutation tests of variable importance were used to calculate Shapley values, which quantify how each predictor contributes to predictions across all observations. Finally, SHAP-based dependence plots were then used to interpret and visualize how each predictor's contribution varies across its observed range. The functions and libraries used are listed in the Supplementary Material (Table S1).

3. Results

3.1 Distribution and color trends in Missouri reservoirs

Averaging across all reservoirs, water color (e.g., λ_d) displays significant interannual variability without a trend (Table 1). On average, reservoirs are green and the annual average range of λ_d (538−555 nm) is closer to the brown, rather than blue, color endmember (Fig. 3a). Interannual variations in hydrometeorological data show that periods of extreme wetness and extreme drought are associated with browner and bluer waters, respectively

(Fig. 3a). Using the most recent LimnoSat data for each reservoir, 94% of Missouri reservoirs are green (n = 451, 94%), compared to 5% brown (n = 24) and less than 1% blue (n = 3).

At the reservoir scale, nearly one third (n = 155) of Missouri reservoirs have had statistically significant shifts in water color (MK analysis, $p < 0.05$), with more (n = 92) negative (e.g., bluer) than positive (n = 63) λ_d trends (Table 1). Regardless of trend direction, shifts in water color were largely confined to the green region of the visible spectrum (Fig. 3b). Almost all reservoirs with negative trends began with λ_d values above 540 nm (Fig. 3c), with 10 reservoirs crossing the 575 nm brown to green threshold, and only one reservoir crossing the 495 nm green to blue threshold. Positive λ_d trends broadly mirror negative λ_d trends, where all reservoirs began green, with only 3 reservoirs crossing the 575 nm green to brown threshold (Fig. 3d).

There are some notable features examining the color and trends of water color across ecoregions and land cover (Table 1, Fig. 4). Using the most recent LimnoSat assessment, the color of reservoirs varied by ecoregion (Kruskal-Wallis; H = 74.85, $p < 0.01$; Fig. 4b) where the mostly forested Ozark Highlands are significantly bluer, although still within the green spectrum, compared to reservoirs in all other ecoregions. Reservoirs with shifts in color occurred across all ecoregions (Table 1); however, the direction and magnitude of these trends did not differ significantly between ecoregions (Kruskal-Wallis; H = 2.15, $p = 0.71$; Fig. 4c). Similarly, the color of reservoirs varied by watershed land cover (Kruskal-Wallis; H = 102.23, $p < 0.01$; Fig. 4d), where reservoirs with forested, mixed, and urban land use are bluer than reservoirs whose watershed is dominated by agriculture and wetlands. Watershed land cover was also a modest predictor of color trends (Kruskal-Wallis; H = 9.98, $p = 0.04$). On average, urban and wetland dominated reservoirs had significant negative and positive trends respectively (Table 1), although high variability within each landcover type precludes significant differences between these watershed land cover types (Fig. 4e).

329 *3.2 Water color and climate variation*

330 A linear mixed-effect model including PDSI, ecoregion, their interaction, and year, accounted for 18% of the
331 explained variation in λ_d measurements across the Missouri LimnoSat record (Table 2). PDSI was significantly
332 correlated with λ_d, such that wet years are associated with higher (i.e., browner) λ_d values, and drought years are
333 associated with lower (i.e., bluer) λ_d values (Fig. 3a); again, largely confined to the green spectral region.
334 Differences in λ_d among reservoirs accounted for approximately 38% of the explained variance (R^2c = 0.56;
335 Table 2). PDSI had significant positive effects on λ_d in Central Irregular Plains, Interior River Valleys, and Hills
336 and Ozark Highlands. The strongest association was observed in the agriculture dominated Central Irregular
337 Plains (slope = 0.968, CI = 0.79 – 1.15), whereas in the Interior River Valleys and Hills (slope = 0.438, CI =
338 0.08 – 0.80) and Ozark Highlands (slope = 0.204, CI = -0.09 – 0.49) changes in PDSI were associated with less
339 pronounced variations in λ_d.
340
341 *3.3 Water color as a trophic status indicator*
342 LimnoSat data was co-located in space and time with a subset of water quality variables that serve as trophic
343 status indicators (Chl *a*, TN, TP, TSS, POM, PIM, DOC, Secchi). All water quality variables are significantly
344 correlated to λ_d (Spearman rank; $p < 0.01$). Chl *a* and DOC are the least correlated (r = 0.42 and r = 0.45,
345 respectively) and Secchi and TP are the most correlated (r = -0.66 and r = 0.63, respectively**)**. To further explore
346 and illustrate these relationships, water quality data were rounded into respective 10 nm λ_d bins and yielded
347 statistically significant differences in median values (Kruskal-Wallis; $p < 0.05$) for all water quality parameters
348 (Fig. 5). Subsequent pairwise analysis (Dunn test using the conservative post-hoc *p*-adjustment Bonferroni
349 method) was performed across a spectral range (485−575 nm) that encompassed >98% of data and yields one
350 blue group (485−495 nm) and 8 green groups ending at the green-brown transition. Overall TP increases with
351 λ_d, but is not significantly different in the 485−555 nm spectral range; however, waterbodies in the 555−565 nm

range have significantly higher TP, that in turn are significantly smaller than TP in waterbodies in the 565−575 nm range. A similar pattern emerges for TN and TSS, with the exception that elevated concentrations of both water quality variables in the two green-brown spectral groups (555−575 nm) are not significantly different from each other. Chl *a* also increases with λ_d and notably peaks before declining at the green-brown transition, with no statistically significant differences between groups. POM, which largely constitutes phytoplankton, follows the same pattern as Chl *a*. PIM, however, shares the same relationship to λ_d and TP, whereby the two brownest waterbody groups are significantly different from each other and from the progressively bluer waterbodies. Secchi depth is the only water quality parameter to form 4 distinct groups. Similar to TP and PIM, Secchi depths are shallower in the brownest waterbody group, are significantly different from the second most brown waterbody group, and waterbodies in the 535−555 nm color range are less transparent than bluer (485-535 nm) waterbodies. Finally, DOC has no significant differences across spectral groups but is generally higher in browner, rather than bluer waters.

3.4 Long-term trends in water quality parameters

Averaging across all sampled reservoirs, several water quality variables including, chl *a*, TN/TP, POM, and the POM/TSS ratio, have significantly increased through time (Table 3). Conversely, hypolimnetic DO, PIM and the PIM/TSS ratio aggregated across all sampled reservoirs, significantly decreased (Table 3). Thus, an overall pattern of moderate eutrophication with diminishing concentrations of inorganic suspended solids has occurred in reservoirs with *in situ* sampling. Amongst the measured physical parameters, surface water temperatures, thermocline depth, and the buoyancy frequency (a metric of stratification intensity), have also increased significantly (Table 3), while hypolimnetic water temperatures have decreased. Chl *a* trends (i.e., slopes) were strongly positively correlated with TN slope ($r = 0.84$), POM slope ($r = 0.92$), and TSS slope ($r = 0.61$), indicating that increases in phytoplankton, nutrients, and suspended materials are correlated (Fig. S4). TSS

trends also had positive correlations with TN slope (r = 0.68), TP (r = 0.61), and POM slope (r = 0.65), while POM trends and TN trends were highly correlated (r = 0.90). Water transparency trends were negatively correlated with TP slope (r = -0.55), PIM slope (r = -0.57) and TSS slope (r = -0.60). TN/TP trends were positively associated with water transparency slope (r = 0.64). Finally, trends in hypoxycline depths were positively correlated with trends in thermocline depth (r = 0.62).

Water quality trends at the scale of individual reservoirs reveal metrics of eutrophication as well as in the direction of oligotrophication (Table 3). TP decreased in twice as many reservoirs (22.3%, *n* = 29) as it increased (11.5%, *n* = 15). TN trends are present in 27.7% (*n* = 36) of reservoirs, with slightly more decreases (*n* = 19) than increases (*n* = 17). The TN/TP ratio changed significantly in 25.4% of reservoirs (*n* = 33), with 16.9% (*n* = 22) showing increases and 8.5% (*n* = 11) decreases, suggesting an overall shift towards increasing phosphorus deficiency. Furthermore, water transparency showed significant changes in 26.2% (*n* = 34) of reservoirs, with slightly more deepening (*n* = 18) than shoaling (*n* = 16) transparency depths. In contrast to these trends indicating that improvements in reservoir water quality are slightly more common than those subject to eutrophication, Chl *a* increased in 27.7% (*n* = 36) of reservoirs and decreased in only 5.4% (*n* = 7). Similarly, TSS increased in 15.8% (*n* = 20) of reservoirs and decreased in 11% (*n* = 14). POM and POM/TSS predominantly increased (33.1%, *n* = 42 and 44.1%, *n* = 56, respectively), while PIM and PIM/TSS decreased (23.6%, *n* = 30 and 42.5%, *n* = 54, respectively). Lastly, significant changes in DOC occurred in 13.3% (*n* = 6) of reservoirs, with increases and decreases distributed evenly.

Surface water temperature exhibited trends in 26.5% of reservoirs (*n* = 22), with the majority showing increases (*n* = 21). In the hypolimnion, 26.5% of reservoirs (*n* = 22) had trends in water temperature, with 16.9% (*n* = 14) experiencing decreases and 9.6% of reservoirs (*n* = 8) experiencing increases. Stratification metrics showed significant changes in some reservoirs, with buoyancy frequency increasing in 47% (*n* = 39) of reservoirs exhibiting trends, whereas no reservoir showed a decreasing trend. Thermocline depth deepened in

12.2% (n = 10) of reservoirs and shoaled in 8.5% (n = 7). Dissolved oxygen (DO) shifts in the epilimnion were distributed evenly, whereas in the hypolimnion, DO predominantly decreased (24.3%, n = 17), with most reservoirs showing no substantial shifts in oxycline nor hypoxycline depths (Table 3).

3.5 Drivers of water color change

Changes in water color ($\Delta\lambda_d$) were explained by a selection of limnological (Chl *a*, Secchi, TP, TN/TP, PIM, POM, TSS, PIM/TSS, POM/TSS, DOC, wtemp, hypolimnion wtemp, thermal stability and dissolved oxygen profile metrics), geomorphological (waterbody and watershed area, waterbody and watershed elongation ratio, Warea/Rarea) and land cover (percent cover of urban, forest, and agriculture lands in the watershed) predictors using BRTs. The final model achieved a MAE of 0.226, a RMSE of 0.295, and an out-of-sample R^2 of 51.7%, evaluated using the independent test set left out during model construction for validation. Overall, waterbody elevation ranked as the most important predictor (RI = 25.76%), followed by urban land cover (RI = 18.33%), waterbody elongation ratio (RI = 13.94%), waterbody area (RI = 11.64%), POM/TSS (RI = 8.50%), watershed area (RI = 5.80%), buoyancy frequency (RI = 5.38%), DOC (RI = 5.36%), and epilimnion DO (RI = 5.29%).

The Shapley-based partial dependence plots for the individual predictors (Figure 6) indicate that reservoirs where λ_d is increasing (i.e., browner) are typically located at lower elevations and in areas with a lower percentage of urban land cover (Fig. 6a–b). Conversely, reservoirs where λ_d is decreasing (i.e., bluer) are found at higher elevations and span a wide range of urban land cover percentages (Fig. 6a–b). In terms of morphology, reservoirs where λ_d is increasing are generally more elongated and have a wide range of waterbody and watershed areas, while reservoirs where λ_d is decreasing are more circular and smaller (Fig. 6c–d, f). Additionally, reservoirs trending towards longer λ_d tend to have intermediate POM/TSS ratios (Fig. 6e), lower thermal stability (Fig. 6g), higher DOC concentrations (Fig. 6h), and intermediate epilimnion DO

concentrations (Fig. 6i). In contrast, reservoirs trending towards shorter λ_d show a broader distribution of POM/TSS ratios (Fig. 6e), stronger summer stratification (Fig. 6g), and lower DOC concentrations (Fig. 6h).

4. Discussion

The dominant wavelength is readily derived from a wide array of earth observing satellites, and water color is perhaps the most easily understood metric for water quality amongst non-experts. While significant effort has been undertaken to estimate optically active water quality parameters (e.g., Chl *a*, DOC, Secchi, TSS) from space (Gholizadeh et al., 2016; Yang et al., 2022), this study adds to a small but growing body of research demonstrating strong linkage between remotely sensed color and other trophic status indicators, most notably TN and TP (Windle et al., 2025). We use λ_d from satellite imagery to investigate the spatial and temporal variability of water color across reservoirs in Missouri and examine how climate, landscape features, waterbody morphology, and physical and chemical limnological properties relate to these trends.

The vast majority of Missouri reservoirs are green; although variations in reservoir color occur across ecoregions and watershed land cover types. Bluer reservoirs are located in the Ozark Highlands and generally have watersheds with forested, mixed, and urban landcovers. The brownest reservoirs occurred mainly in agricultural and wetland watersheds that have high nutrient concentrations, elevated levels of inorganic suspended sediment, high DOC, and low water transparency. In Missouri, agricultural watersheds tend to have greater soil organic matter stores than forested watersheds (Jones et al., 2008b) that result in elevated terrestrial CDOM in reservoirs (Bhattacharya et al., 2022), particularly during periods of high precipitation. This is consistent with previous studies showing that Missouri reservoirs in agricultural watersheds are more eutrophic than forested watersheds (Jones et al., 2008b), as well as continental-scale patterns showing a high prevalence of green and brown eutrophic waterbodies in agricultural Midwest regions (Oliver et al., 2017).

Interannual variations in hydrometeorological conditions are significantly correlated with λ_d, such that wet years are associated with higher λ_d values (browner) and drought years are associated with lower λ_d values (bluer). Increased runoff during wet conditions transports greater amounts of terrestrially derived substances – both inorganic (e.g., sediments and nutrients) and organic (e.g., dissolved organic carbon) – into reservoirs that collectively shift λ_d to longer wavelengths (De Wit et al., 2016). The effect of hydrological cycles in controlling nutrients (Jones et al., 2008a) and CDOM (Bhattacharya et al., 2022) has been previously explored in Missouri reservoirs, with wet summers increasing watershed-derived inputs. That said, incorporation of ecoregions into a linear mixed-effect model emerged as an important predictor explaining the covariation of PDSI and λ_d. Notably, reservoirs in the forested Ozark Highlands become bluer during wet conditions, suggesting that high precipitation events act more to dilute rather than import nutrients and other optically active constituents. In this framework, the absence or presence of water level management across reservoirs is likely an important co-factor driving hydrometeorological control of water color.

Long-term trends in water color and quality

Nearly one-third of the reservoirs displayed trends in water color, of which approximately 60% shifted toward shorter λ_d (n = 92; bluer). The majority of these reservoirs either remained green (n = 81) or shifted from brown to green waters (n = 10), suggesting a recovery from more turbid conditions. These changes in water color broadly align with trends in *in situ* water quality parameters, where reservoirs with diminishing TN, TP, PIM, and increasing water transparency are more common than reservoirs with opposite trends (Fig. S5). Yet despite this general correspondence, Chl *a* and POM, both proxies for phytoplankton biomass, increased rather than decreased in more reservoirs in contrast to previous studies that show declines in λ_d are often associated with reductions in Chl *a* concentrations (Lehmann et al., 2018). Earlier studies have found that particulate inorganic matter (PIM) in Missouri reservoirs is typically the dominant fraction of total suspended solids (TSS),

particularly in agricultural watersheds due to erosion and runoff (Jones et al., 2008b; Jones and Knowlton, 2005). However, more recent studies have found that particulate organic matter (POM) concentrations now exceed those of PIM in these systems (Petty et al., 2020). Our results support this shift, showing a recent trend of increasing POM and decreasing PIM, indicating a shift in the particulate load from sediment particles. Thus, general parallel shifts towards bluer (less brown) waters and higher concentrations of POM and Chl *a* are consistent with diminished PIM, and may be alleviating light limitation of phytoplankton communities. Given that the majority of significant trends (both negative and positive) are confined within the green spectral region closer to the brown rather blue spectral end member, and that in these color regions TP, PIM, and Secchi depth but not Chl *a* nor POM co-vary with λ_d (Fig. 5) demonstrates that diminished λ_d can in fact correspond to elevated phytoplankton biomass. This finding also supports that erosion control resulting from the statewide implementation of best management practices (e.g., shoreline stabilization with rock and water willow; Jones et al., 2022) has resulted in diminished PIM and shifts in water color in many reservoirs.

Landscape and morphological drivers of water color trends

Water color trends in Missouri reservoirs were primarily associated with climate, landscape features (elevation, urban land cover, watershed area), reservoir morphology (e.g., area and shape), and limnological parameters (particulate organic and inorganic matter, dissolved organic carbon, stratification index and epilimnion DO). While previous studies have linked water color changes to climatic conditions, landscape properties and waterbody morphology (Cao et al., 2023; Oleksy et al., 2022; Shen et al., 2025), these previous studies lacked *in-situ* physical and chemical parameters. Our findings reinforce the importance of integrating water quality data when analyzing trends in water color, as water quality parameters alone contributed 24.5% of the total relative importance among significant predictors in the BRT analysis. Specifically, the inclusion of water

quality parameters provides a critical link between landscape and morphological features and the internal limnological processes that mediate long-term trends in water color.

Waterbody elevation consistently ranked as the most important predictor in our models, revealing that reservoirs trending toward bluer wavelengths are generally situated at higher elevations compared to those trending toward greener wavelengths, consistent with other regional analysis (Cao et al., 2023) with a noted exception of high alpine environments (Oleksy et al., 2022). Urban land cover ranked as the second most important predictor in our BRT model. Although urbanization can increase chemical and thermal pollution in freshwater ecosystems (Grimm et al., 2008), we found that reservoirs tending toward shorter λ_d occurred in regions where urban cover ranged from 20 to 80%. Oleksy et al. (2022) similarly found that reservoirs trending towards bluer waters were primarily located in areas with a higher percentage of urban land cover. A potential explanation is that local management practices during the summer may drive changes in water color without necessarily indicating improvements in overall water quality. In Missouri, multiple reservoirs are managed to optimize recreational fisheries by removing macrophytes through the introduction of benthivorous fish (e.g., grass carp) and herbicide (e.g., glyphosate) applications (Jones et al., 2022). Interventions such as applications of nutrient-containing herbicides can reduce Chl *a* concentrations in the short term by suppressing phytoplankton growth through decreased efficiency of photosystem II (Lürling and Roessink, 2006), consequently resulting in shifts toward shorter λ_d. However, over the long term, these treatments often increase nutrient availability in aquatic ecosystems, primarily due to nitrogen and phosphorus content present in these chemicals (Reinl et al., 2022). Waterbody and watershed area, along with waterbody shape, consistently ranked as important predictors in our models. Reservoirs trending toward shorter λ_d are generally more circular and small. These smaller reservoirs also exhibited greater variability in the magnitude of water color change. This pattern aligns with findings that smaller waterbodies are more susceptible to color changes (Shen et al., 2025).

Collectively, these interactions between morphology and landscape features may help explain the spatial variation observed in water color trends.

5. Conclusion

Shifts in water color and suspended solids composition likely reflect changes in watershed land use and reservoir management practices, which have contributed to reductions in particulate inorganic matter and, ultimately, influenced apparent water color. Climate projections indicate increasing frequency and intensity of droughts across the study region (Strzepek et al., 2010). Under such conditions, our findings suggest that reservoirs in the Midwest are likely to shift toward shorter visual wavelengths (i.e., greening), potentially altering primary productivity and energy transfer within these man-made systems. The observed reduction in brown color reservoirs suggests improvements in water quality in recent years in historically turbid reservoirs, although decreasing trends remained within the green region of the visible spectrum. The absence of an overall trend, coupled with contrasting reservoir-level water color trends, underscores that local forces, rather than broad regional drivers, are primarily responsible for the observed changes in water color.

Satellite-derived water color offers a practical tool for assessing how upstream land use and local best management practices (BMPs) affect water quality at the reservoir scale. In a time of reduced federal funding for long-term water quality monitoring programs, our findings underscore the value of satellite-based assessments as a cost-effective and scalable approach to monitor water quality trends over time and space. Many remote-sensing products are now freely available, offering a wide range of spatial (1m – 1 km) and temporal (1 – 15 days) resolutions, and therefore can provide critical information on water quality trends even in regions with limited environmental monitoring (Smits et al., 2025). Moreover, monitoring programs can be strategically redesigned to improve data coverage by selecting key site locations and leveraging remote sensing to interpolate data across time and space (Smits et al., 2025). However, we emphasize the continued importance

of field-based observations to ensure accuracy, validate remote sensing products, and maintain the integrity of water quality assessments.

Acknowledgments

This research was supported by NASA grant 80NSSC22K0771 (*Remote Sensing of Water Quality*) awarded to R.L.N and G.M.S. The data is based on work supported by the Missouri Department of Natural Resources (MDNR), which funds the Missouri Statewide Lake Assessment Program (SLAP), coordinated by the University of Missouri (MU) Limnology Laboratory. Part of the data was also obtained through the Lakes of Missouri Volunteer Program (LMVP) funded by MDNR, whose contributions are gratefully acknowledged. The graphical abstract was produced as part of work supported by the Prairie Fork Conservation Area (PFCA), managed by the Missouri Department of Conservation, under funding awarded to L.P.S., R.L.B., and G.M.S. The authors are deeply grateful to all students and technicians associated with the MU Limnology Lab over the years, whose efforts in collecting, processing, and analyzing the water quality data made this research possible. We also thank Dr. Xiaoxu Guo for reviewing the BRT analysis code and offering valuable feedback on our approach.

6. References

Bhattacharya, R., Jones, J.R., Graham, J.L., Obrecht, D. V., Thorpe, A.P., Harlan, J.D., North, R.L., 2022. Nonlinear multidecadal trends in organic matter dynamics in Midwest reservoirs are a function of variable hydroclimate. Limnol Oceanogr 67, 2531–2546.

Binding, C.E., Jerome, J.H., Bukata, R.P., Booty, W.G., 2007. Trends in water clarity of the lower Great Lakes from remotely sensed aquatic color. J Great Lakes Res 33, 828–841.

Cao, F., Tzortziou, M., Hu, C., Mannino, A., Fichot, C.G., Del Vecchio, R., Najjar, R.G., Novak, M., 2018. Remote sensing retrievals of colored dissolved organic matter and dissolved organic carbon dynamics in North American estuaries and their margins. Remote Sens Environ 205, 151–165.

Cao, Z., Melack, J.M., Liu, M., Kutser, T., Duan, H., Ma, R., 2023. Shifts, trends, and drivers of lake color across China since the 1980s. Geophys Res Lett 50, e2023GL103225.

Charifson, D.M., Huth, P.C., Thompson, J.E., Angyal, R.K., Flaherty, M.J., Richardson, D.C., 2015. History of fish presence and absence following lake acidification and recovery in Lake Minnewaska, Shawangunk Ridge, NY. Northeast Nat (Steuben) 22, 762–781.

De Wit, H.A., Valinia, S., Weyhenmeyer, G.A., Futter, M.N., Kortelainen, P., Austnes, K., Hessen, D.O., Räike, A., Laudon, H., Vuorenmaa, J., 2016. Current browning of surface waters will be further promoted by wetter climate. Environ Sci Technol Lett 3, 430–435.

Dodds, W.K., Bouska, W.W., Eitzmann, J.L., Pilger, T.J., Pitts, K.L., Riley, A.J., Schloesser, J.T., Thornbrugh, D.J., 2009. Eutrophication of U. S. freshwaters: Analysis of potential economic damages. Environ Sci Technol 43, 12–19.

Dogliotti, A.I., Ruddick, K.G., Nechad, B., Doxaran, D., Knaeps, E., 2015. A single algorithm to retrieve turbidity from remotely-sensed data in all coastal and estuarine waters. Remote Sens Environ 156, 157–168.

569 Elith, J., Leathwick, J.R., Hastie, T., 2008. A working guide to boosted regression trees. Journal of Animal
570 Ecology 77, 802–813.
571 Erlandsson, M., Buffam, I., Fölster, J., Laudon, H., Temnerud, J., Weyhenmeyer, G.A., Bishop, K., 2008. Thirty-
572 five years of synchrony in the organic matter concentrations of Swedish rivers explained by variation in flow
573 and sulphate. Glob Chang Biol 14, 1191–1198.
574 Freeman, C., Evans, C.D., Monteith, D.T., Reynolds, B., Fenner, N., 2001. Export of organic carbon from peat
575 soils. Nature 412, 785–785.
576 Gholizadeh, M.H., Melesse, A.M., Reddi, L., 2016. A comprehensive review on water quality parameters
577 estimation using remote sensing techniques. Sensors 16, 1298.
578 Grimm, N.B., Faeth, S.H., Golubiewski, N.E., Redman, C.L., Wu, J., Bai, X., Briggs, J.M., 2008. Global change
579 and the ecology of cities. Science 319, 756–760.
580 Hongve, D., Riise, G., Kristiansen, J.F., 2004. Increased colour and organic acid concentrations in Norwegian
581 forest lakes and drinking water - A result of increased precipitation? Aquat Sci 66, 231–238.
582 Jeppesen, E., Søndergaard, M., Jensen, J.P., Havens, K.E., Anneville, O., Carvalho, L., Coveney, M.F., Deneke,
583 R., Dokulil, M.T., Foy, B., Gerdeaux, D., Hampton, S.E., Hilt, S., Kangur, K., Köhler, J., Lammens,
584 E.H.H.R., Lauridsen, T.L., Manca, M., Miracle, M.R., Moss, B., Nõges, P., Persson, G., Phillips, G.,
585 Portielje, R., Romo, S., Schelske, C.L., Straile, D., Tatrai, I., Willén, E., Winder, M., 2005. Lake responses
586 to reduced nutrient loading - An analysis of contemporary long-term data from 35 case studies. Freshw Biol
587 50, 1747–1771.
588 Jones, J.R., Knowlton, M.F., 2005. Suspended solids in Missouri reservoirs in relation to catchment features and
589 internal processes. Water Res 39, 3629–3635.

590 Jones, J.R., Knowlton, M.F., Obrecht, D. V., 2008a. Role of land cover and hydrology in determining nutrients
591 in mid-continent reservoirs: Implications for nutrient criteria and management. Lake Reserv Manag 24, 1–
592 9.
593 Jones, J.R., Obrecht, D., North, R.L., 2022. Influence of fisheries and shoreline management on limnological
594 characteristics of three Missouri reservoirs. Inland Waters 12, 354–367.
595 Jones, J.R., Obrecht, D. V., Perkins, B.D., Knowlton, M.F., Thorpe, A.P., Watanabe, S., Bacon, R.R., 2008b.
596 Nutrients, seston, and transparency of Missouri reservoirs and oxbow lakes: An analysis of regional
597 limnology. Lake Reserv Manag 24, 155–180.
598 Leech, D.M., Pollard, A.I., Labou, S.G., Hampton, S.E., 2018. Fewer blue lakes and more murky lakes across the
599 continental U.S.: Implications for planktonic food webs. Limnol Oceanogr 63, 2661–2680.
600 Lehmann, M.K., Nguyen, U., Allan, M., van der Woerd, H.J., 2018. Colour classification of 1486 lakes across a
601 wide range of optical water types. Remote Sens 10, 1273.
602 Li, J., Wang, J., Wu, Y., Cui, Y., Yan, S., 2022. Remote sensing monitoring of total nitrogen and total phosphorus
603 concentrations in the water around Chaohu Lake based on geographical division. Front Environ Sci 10,
604 1014155.
605 Lürling, M., Roessink, I., 2006. On the way to cyanobacterial blooms: Impact of the herbicide metribuzin on the
606 competition between a green alga (Scenedesmus) and a cyanobacterium (Microcystis). Chemosphere 65,
607 618–626.
608 McKibben, S.M., Schollaert Uz, S., Palacios, S.L., 2024. Testing a Hyperspectral, bio-optical approach to
609 identification of phytoplankton community composition in the Chesapeake Bay estuary. Earth and Space
610 Science 11, e2023EA003244.

611 Monteith, D.T., Stoddard, J.L., Evans, C.D., De Wit, H.A., Forsius, M., Høgåsen, T., Wilander, A., Skjelkvåle,
612 B.L., Jeffries, D.S., Vuorenmaa, J., Keller, B., Kopécek, J., Vesely, J., 2007. Dissolved organic carbon trends
613 resulting from changes in atmospheric deposition chemistry. Nature 450, 537–540.
614 Mouw, C.B., Greb, S., Aurin, D., DiGiacomo, P.M., Lee, Z., Twardowski, M., Binding, C., Hu, C., Ma, R.,
615 Moore, T., Moses, W., Craig, S.E., 2015. Aquatic color radiometry remote sensing of coastal and inland
616 waters: Challenges and recommendations for future satellite missions. Remote Sens Environ. 160, 15–30.
617 Nakagawa, S., Schielzeth, H., 2013. A general and simple method for obtaining R^2 from generalized linear mixed-
618 effects models. Methods Ecol Evol 4, 133–142.
619 Oleksy, I.A., Collins, S.M., Sillen, S.J., Topp, S.N., Austin, M., Hall, E.K., O'Reilly, C.M., Yang, X., Ross,
620 M.R.V., 2022. Heterogenous controls on lake color and trends across the high-elevation U.S. Rocky
621 Mountain region. Environmental Research Letters 17, 104041.
622 Oleksy, I.A., Solomon, C.T., Jones, S.E., Olson, C., Bertolet, B.L., Adrian, R., Bansal, S., Baron, J.S., Brothers,
623 S., Chandra, S., Chou, H.M., Colom-Montero, W., Culpepper, J., de Eyto, E., Farragher, M.J., Hilt, S.,
624 Holeck, K.T., Kazanjian, G., Klaus, M., Klug, J., Köhler, J., Laas, A., Lundin, E., Parkes, A.H., Rose, K.C.,
625 Rustam, L.G., Rusak, J., Scordo, F., Vanni, M.J., Verburg, P., Weyhenmeyer, G.A., 2024. Controls on lake
626 pelagic primary productivity: Formalizing the nutrient-color paradigm. J Geophys Res Biogeosci 129,
627 e2024JG008140.
628 Oliver, S.K., Collins, S.M., Soranno, P.A., Wagner, T., Stanley, E.H., Jones, J.R., Stow, C.A., Lottig, N.R., 2017.
629 Unexpected stasis in a changing world: Lake nutrient and chlorophyll trends since 1990. Glob Chang Biol
630 23, 5455–5467.
631 Ondrusek, M., Stengel, E., Kinkade, C.S., Vogel, R.L., Keegstra, P., Hunter, C., Kim, C., 2012. The development
632 of a new optical total suspended matter algorithm for the Chesapeake Bay. Remote Sens Environ 119, 243–
633 254.

634 Petty, E.L., Obrecht, D. V., North, R.L., 2020. Filling in the Flyover Zone: High Phosphorus in Midwestern
635 (USA) Reservoirs Results in High Phytoplankton Biomass but Not High Primary Productivity. Front Environ
636 Sci 8, 111.
637 Reinl, K.L., Harris, T.D., Elfferich, I., Coker, A., Zhan, Q., De Senerpont Domis, L.N., Morales-Williams, A.M.,
638 Bhattacharya, R., Grossart, H.P., North, R.L., Sweetman, J.N., 2022. The role of organic nutrients in
639 structuring freshwater phytoplankton communities in a rapidly changing world. Water Res 219, 118573.
640 Roulet, N., Moore, T.R., 2006. Environmental chemistry: Browning the waters. Nature 444, 283–284.
641 Schindler, D.W., Hecky, R.E., McCullough, G.K., 2012. The rapid eutrophication of Lake Winnipeg: Greening
642 under global change. J Great Lakes Res 38, 6–13.
643 Shen, X., Ke, C.Q., Duan, Z., Cai, Y., Li, H., Xiao, Y., 2025. Satellite observations reveal widespread color
644 variations in global lakes since the 1980s. Water Resour Res 61, e2023WR036926.
645 Sillen, S.J., Ross, M.R.V., Collins, S.M., 2024. Long-Term Trends in Productivity Across Intermountain West
646 Lakes Provide No Evidence of Widespread Eutrophication. Water Resour Res 60, e2023WR034997.
647 Smith, B., Pahlevan, N., Schalles, J., Ruberg, S., Errera, R., Ma, R., Giardino, C., Bresciani, M., Barbosa, C.,
648 Moore, T., Fernandez, V., Alikas, K., Kangro, K., 2020. A chlorophyll-a algorithm for Landsat-8 based on
649 mixture density networks. Frontiers in Remote Sensing 1, 623678.
650 Smits, A.P., Hall, E.K., Deemer, B.R., Scordo, F., Barbosa, C.C., Carlson, S.M., Cawley, K., Grossart, H.P.,
651 Kelly, P., Mammola, S., Pintar, M.R., Robbins, C.J., Ruhi, A., Saccò, M., 2025. Too much and not enough
652 data: Challenges and solutions for generating information in freshwater research and monitoring. Ecosphere
653 16, e70205.
654 Strzepek, K., Yohe, G., Neumann, J., Boehlert, B., 2010. Characterizing changes in drought risk for the United
655 States from climate change. Environmental Research Letters 5, 044012.

Sukristiyanti, S., Maria, R., Lestiana, H., 2018. Watershed-based Morphometric Analysis: A Review. In: IOP Conference Series: Earth and Environmental Science. Institute of Physics Publishing 118, 012028.

Topp, S., Pavelsky, T., Yang, X., Gardner, J., Rossa, M.R. V, 2020. LimnoSat-US: A Remote Sensing Dataset for U.S. Lakes from 1984-2020. https://doi.org/10.5281/zenodo.4139695.

Topp, S.N., Pavelsky, T.M., Dugan, H.A., Yang, X., Gardner, J., Ross, M.R.V., 2021. Shifting Patterns of Summer Lake Color Phenology in Over 26,000 US Lakes. Water Resour Res 57, e2020WR029123.

Vanhellemont, Q., 2019. Adaptation of the dark spectrum fitting atmospheric correction for aquatic applications of the Landsat and Sentinel-2 archives. Remote Sens Environ 225, 175–192.

Wang, S., Li, J., Shen, Q., Zhang, B., Zhang, F., Lu, Z., 2015. MODIS-Based radiometric color extraction and classification of inland water with the forel-ule scale: A case study of lake Taihu. IEEE J Sel Top Appl Earth Obs Remote Sens 8, 907–918.

Williamson, C.E., Morris, D.P., Pace, M.L., Olson, O.G., 1999. Dissolved organic carbon and nutrients as regulators of lake ecosystems: Resurrection of a more integrated paradigm. Limnol Oceanogr 44, 795–803.

Windle, A.E., Malkin, S.Y., Hood, R.R., Silsbe, G.M., 2025. Optical water typing in optically complex waters: A case study of Chesapeake Bay. Science of the Total Environment 981, 179558.

Woolway, R.I., Kraemer, B.M., Lenters, J.D., Merchant, C.J., O'Reilly, C.M., Sharma, S., 2020. Global lake responses to climate change. Nat Rev Earth Environ 1, 388–403.

Xiong, J., Lin, C., Cao, Z., Hu, M., Xue, K., Chen, X., Ma, R., 2022. Development of remote sensing algorithm for total phosphorus concentration in eutrophic lakes: Conventional or machine learning? Water Res 215, 118213.

Yang, H., Kong, J., Hu, H., Du, Y., Gao, M., Chen, F., 2022. A Review of Remote Sensing for Water Quality Retrieval: Progress and Challenges. Remote Sens 14, 1770.

678 **Table 1:** Dominant wavelength (λd; mean ± SD) and its trend (Δλd; mean ± SD) summarizing overall changes
679 and shifts toward shorter λd (i.e., greener or bluer waters) and longer λd (i.e., greener or browner waters) across
680 ecoregions and land cover groups in Missouri. For shorter and longer λd, only significant trends (*p*-value ≤
681 0.05) are reported. *n* indicates the number of reservoirs; SD is standard deviation.

	First year λd (nm)	Last year λd (nm)	Regional Scale			Reservoir Scale			
			Overall Trend			Shorter λd		Longer λd	
			n	Sen's Slope (nm yr^{-1})	*p*-value	*n*	Sen's Slope (nm yr^{-1})	*n*	Sen's Slope (nm yr^{-1})
All reservoirs			478	-0.001	0.990	92	-0.492±0.290	63	0.390±0.251
Ecoregion									
Ozark Highlands	538.9	540.8	149	0.000	1.000	28	-0.567±0.339	14	0.566±0.257
Central Irregular Plains	561.0	560.7	196	-0.033	0.647	42	-0.440±0.242	27	0.349±0.211
Western Corn Belt Plains	563.6	562.7	42	-0.009	0.784	7	-0.457±0.311	8	0.392±0.378
Interior River Valleys and Hills	549.0	551.7	69	-0.063	0.244	12	-0.569±0.307	12	0.292±0.150
Mississippi Alluvial Plain	561.2	555.9	21	-0.001	1.000	3	-0.291±0.150	2	0.296±0.204
Mississippi Valey Loess Plains	560.5	561.5	1	-0.056	0.231	0	-	0	-
Land cover									
Agriculture	559.8	561.1	218	-0.024	0.610	44	-0.425±0.255	31	0.309±0.186
Forest	539.7	542.0	141	-0.044	0.610	23	-0.634±0.341	11	0.550±0.242
Mixed	551.7	548.9	85	0.033	0.381	15	-0.439±0.238	15	0.420±0.311
Urban	553.6	539.5	22	-0.159	**0.004**	10	-0.540±0.292	3	0.346±0.168
Wetland	563.5	568.4	11	0.152	**0.003**	0	-	3	0.535±0.399
Open Water	528.3	515.4	1	0.503	0.259	0	-	0	-

682

683 **Table 2:** Linear mixed-effect model of relationships between dominant wavelength (λ_d; response variable),
684 Palmer drought severity index (PDSI; predictor), and ecoregions in Missouri. In the model, year is included as a
685 numeric covariate and reservoirs' ID as a random term. R^2m and R^2c refer to marginal (only fixed terms) and
686 conditional (fixed and random terms) adjusted R^2, respectively.

Fixed effects	**Estimates**	**SE**	**95% CI**	**t-values**	***p*-values**	R^2m	R^2c
Intercept	768.71	45.17	680.16 – 857.27	17.02	**< 0.001**	0.181	0.560
PDSI	0.97	0.09	0.79 – 1.15	10.44	**< 0.001**		
Year	-0.11	0.02	-0.15 – -0.06	-4.83	**< 0.001**		
Interior River Valleys and Hills	-5.07	3.15	-11.26 – 1.11	-1.61	0.108		
Mississippi Alluvial Plain	6.79	15.59	-23.78 – 37.36	0.44	0.663		
Ozark Highlands	-20.92	2.54	-25.91 – -15.93	-8.22	**< 0.001**		
Western Corn Belt Plains	-4.94	4.03	-12.85 – 2.97	-1.22	0.221		
PDSI:Interior River Valleys and Hills	-0.53	0.21	-0.93 – -0.13	-2.58	**0.010**		
PDSI:Mississippi Alluvial Plain	-3.93	3.05	-9.91 – 2.05	-1.29	0.197		
PDSI:Ozark Highlands	-0.76	0.17	-1.11 – -0.42	-4.38	**< 0.001**		
PDSI:Western Corn Belt Plains	-0.23	0.21	-0.63 – 0.18	-1.10	0.271		
Radom effects							
Reservoir identity	12.74						

687

688 **Table 3:** Sen's slope estimates (mean ± SD) for overall trend and reservoirs with increasing or decreasing
689 trends in water quality parameters. For the overall trend, *n* indicates the number of reservoirs with at least 10
690 consecutive years of data. For increasing and decreasing trends, only reservoirs that exhibited significant
691 changes (*p*-value ≤ 0.05) are included, and *n* represents the number of such reservoirs. SD is standard deviation.
692 DOC refers to dissolved organic carbon, POM to particulate organic matter, PIM to particulate inorganic matter,
693 TSS to total suspended solids, DO to dissolved oxygen, and wtemp to water temperature.

		Regional Scale			**Reservoir Scale**			
		Overall trend			**Decreasing trend**		**Increasing trend**	
		n	**Sen's Slope (year^{-1})**	***p-value***	***n***	**Sen's Slope (year^{-1})**	***n***	**Sen's Slope (year^{-1})**
Biogeochemical								
Chlorophyll *a*	µg/L	130	0.286	**<0.001**	7	-1.37±1.26	36	1.59±1.81
Secchi depth	m	130	-0.001	0.609	16	-0.05±0.04	18	0.05±0.04
Total nitrogen (TN)	µmol/L	130	0.108	0.118	19	-0.82±0.54	17	1.21±1.02
Total phosphorus (TP)	µmol/L	130	0.004	0.258	29	-0.03±0.02	15	0.11±0.16
TN/TP	-	130	0.195	**0.034**	11	-1.09±0.76	22	1.33±1.30
DOC	µmol/L	45	-3.368	0.484	3	-16.4±4.84	2	13.0±4.07
POM	mg/L	127	0.043	**<0.001**	7	-0.20±0.29	42	0.16±0.17
PIM	mg/L	127	-0.054	**<0.001**	30	-0.14±0.17	13	0.28±0.20
TSS	mg/L	127	-0.006	0.833	14	-0.27±0.29	20	0.33±0.31
POM/TSS	-	127	0.006	**<0.001**	9	-0.02±0.01	56	0.01±0.01
PIM/TSS	-	127	-0.006	**<0.001**	54	-0.01±0.01	9	0.02±0.01
Epilimnion DO	mg/L	70	-0.022	0.208	5	-0.16±0.10	5	0.12±0.08
Hypolimnion DO	mg/L	70	-0.032	**0.001**	17	-0.12±0.10	1	0.19±0.00
Physical								
Surface wtemp	℃	83	0.050	**0.010**	1	-0.22±0.00	21	0.16±0.12
Buoyancy frequency	s^{-2}	83	$2x10^{-4}$	**<0.001**	0	-	39	$5x10^{-4}$±$9.3x10^{-4}$
Thermocline depth	m	82	0.019	**0.002**	7	-0.08±0.06	10	0.10±0.09
Hypolimnion wtemp	℃	83	-0.044	**0.004**	14	-0.29±0.37	8	0.27±0.18
Oxycline depth	m	70	-0.003	0.659	2	-0.10±0.03	2	0.11±0.01
Hypoxycline depth	m	62	0.004	0.634	11	-0.10±0.07	2	0.13±0.07

694

695 **Figure captions**

696 **Figure 1:** Map of a) Missouri (United States) reservoirs showing available *in situ* and/or LimnoSat time series
697 embedded across the state's six Environmental Protection Agency (EPA) ecoregions (Ozark Highlands, Central
698 Irregular Plains, Western Corn Belt Plains, Interior River Valleys and Hills, Mississippi Alluvial Plain, and the
699 Mississippi Valley Loess Plains), and b) predominant watershed land cover types of the studied reservoirs based
700 on 2021 NLCD data.

701

702 **Figure 2:** Flowchart illustrating the processing and analysis of climatic (Palmer Drought Severity Index; PDSI),
703 remotely-sensed (LimnoSat), *in situ* water quality (WQ), reservoir morphology and watershed land cover data.
704 LMM refers to linear mixed-effect models, BRT refers to boosted regression tree, and *n* refers to the number of
705 reservoirs included in each dataset or analysis. Water quality parameters include chlorophyll *a* (chl *a*), Secchi
706 disk depth (Secchi), total nitrogen (TN), total phosphorus (TP), total nitrogen to total phosphorus ratio (TN/TP),
707 particulate organic matter (POM), particulate inorganic matter (PIM), total suspended solids (TSS), surface
708 water temperature (wtemp), hypolimnion water temperature (hypo wtemp), buoyancy frequency (buoy freq),
709 thermocline depth (thermocline), dissolved oxygen (DO) profile metrics (epilimnion DO, hypolimnion DO,
710 oxycline and hypoxycline), and dissolved organic carbon (DOC).

711

712 **Figure 3:** a) Annual mean dominant wavelength (λ_d) for all reservoirs (solid line) and grouped by trend
713 category (increasing and decreasing λ_d; dashed lines) from 1984 to 2020. Colors correspond to PDSI index:
714 light blue represents moderately wet years (PDSI > 0), dark blue indicates extremely wet years (PDSI ≥ +3),
715 light brown indicates moderately dry years (PDSI < 0), and dark brown represents extreme drought conditions
716 (PDSI ≤ -3). Graphs b–d represent the number of reservoirs distributed across λ_d (binned in 5 nm intervals) in

717 the first and last years between 1984 and 2020; b) all reservoirs; c) reservoirs trending toward shorter λ_d; d)
718 reservoirs trending toward longer λ_d. Horizontal dashed lines in graphs b–d represent the mean λ_d.
719
720 **Figure 4:** a) Distribution of reservoir dominant wavelength (λ_d) across the state's six Environmental Protection
721 Agency (EPA) ecoregions, box and whisker plot of b) λ_d in recent years (i.e., last year for each reservoir) by
722 ecoregions, c) dominant wavelength slope (i.e., change; $\Delta\lambda_d$) by ecoregion, d) λ_d in recent years by watershed
723 land cover types, and e) $\Delta\lambda_d$ by watershed land cover types. Different letters represent the significant differences
724 (p-values ≤ 0.05) in λ_d and $\Delta\lambda_d$ between ecoregions (b–c) and watershed land cover types (d–e) based on
725 pairwise Dunn's tests with Bonferroni-adjusted *p*-values.
726
727 **Figure 5:** Box and whisker plot showing the matchups between *in situ* water quality parameters and dominant
728 wavelength (λ_d) values binned in 10 nm intervals. Graphs a–h correspond to different water quality parameters:
729 a) total phosphorus (TP), b) total nitrogen (TN), c) chlorophyll *a* (Chl *a*), d) total suspended solids (TSS), e)
730 particulate organic matter (POM), f) particulate inorganic matter (PIM), g) Secchi disk depth, and h) dissolved
731 organic carbon (DOC). Different letters within each graph represent significant differences (*p*-values ≤ 0.05)
732 among λ_d bins based on pairwise Dunn's tests with Bonferroni-adjusted *p*-values.
733
734 **Figure 6:** Shapley-based dependence plots for the most important variables selected by the BRT model. Each
735 graph shows how the values of a given predictor (x-axis) influence the model's prediction of the dominant
736 wavelength slope ($\Delta\lambda_d$), as represented by the SHAP values (y-axis). Positive SHAP values indicate a
737 contribution to increasing $\Delta\lambda_d$ (brown dots), while negative values indicate a contribution to decreasing $\Delta\lambda_d$
738 (green dots) across the study reservoirs. Graphs a–i correspond to different parameters: a) water body elevation,
739 b) urban land cover, c) water body elongation ratio, d) water body area, e) particulate organic matter to total

suspended solids ratio (POM/TSS), f) watershed area, g) buoyancy frequency, h) dissolved organic carbon (DOC), and i) epilimnion dissolved oxygen (DO). RI refers to average relative importance ranked by the selected BRT model. Only significant predictors are shown.

Graphical abstract

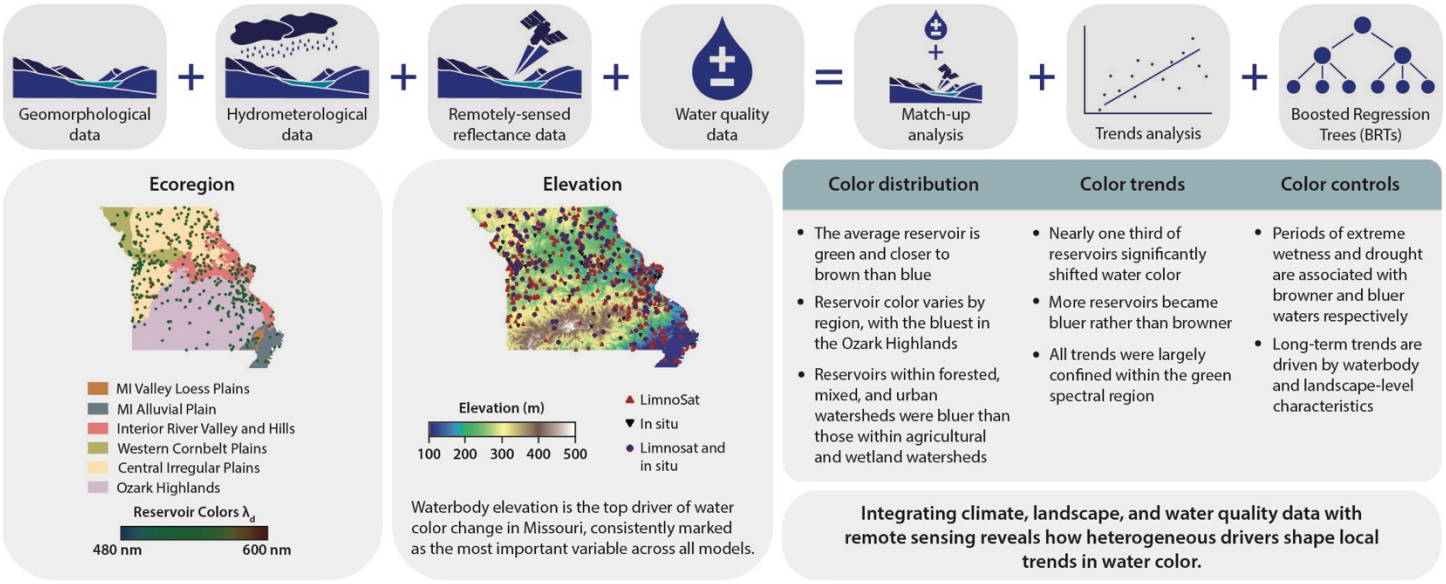

745 **Figure 1**

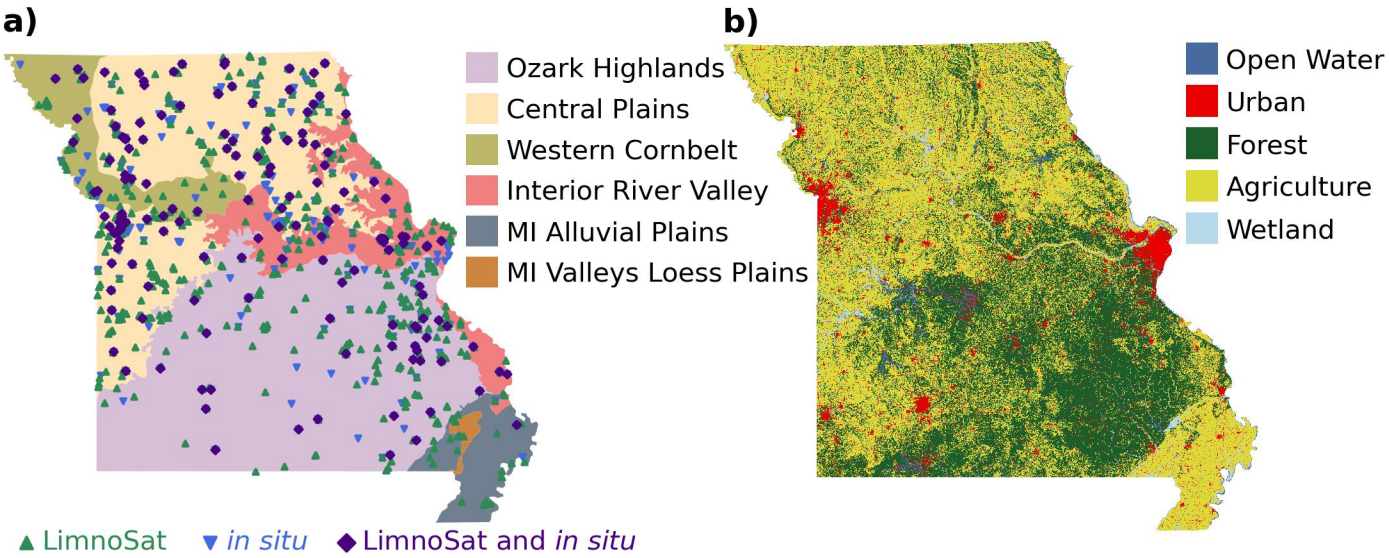

746

747 **Figure 2**

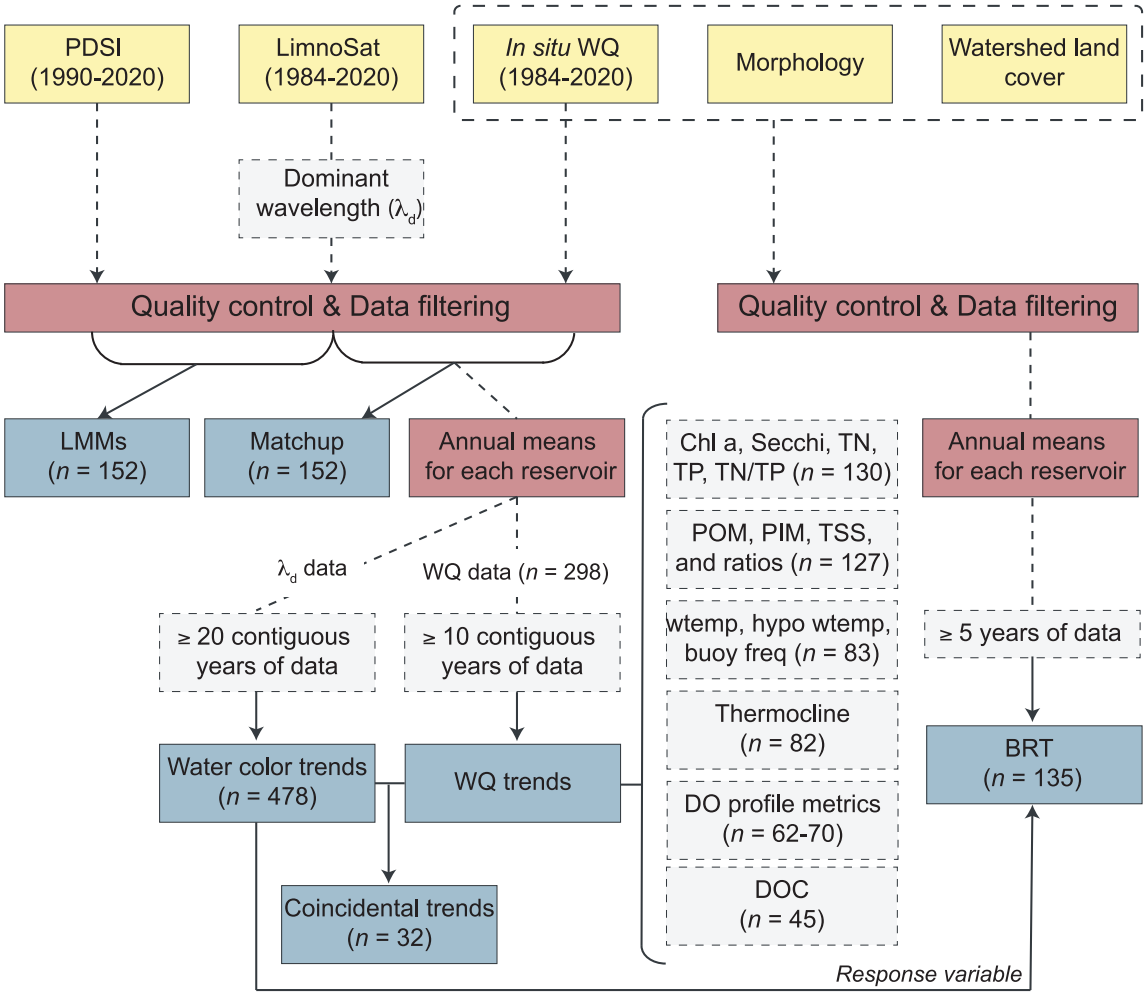

748

Figure 3

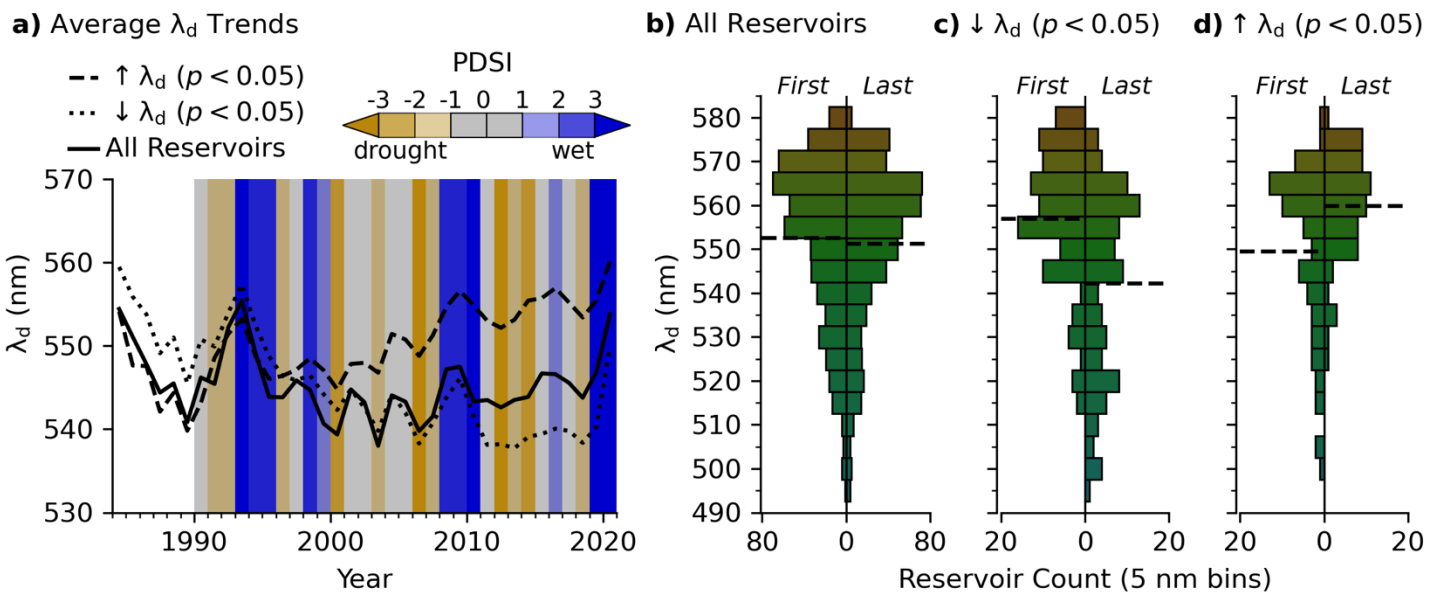
a) Average λd Trends
↑ λd (p < 0.05)
↓ λd (p < 0.05)
All Reservoirs
PDSI
-3 -2 -1 0 1 2 3
drought
wet
λd (nm)
Year
b) All Reservoirs
c) ↓ λd (p < 0.05)
d) ↑ λd (p < 0.05)
First
Last
Reservoir Count (5 nm bins)

751 **Figure 4**

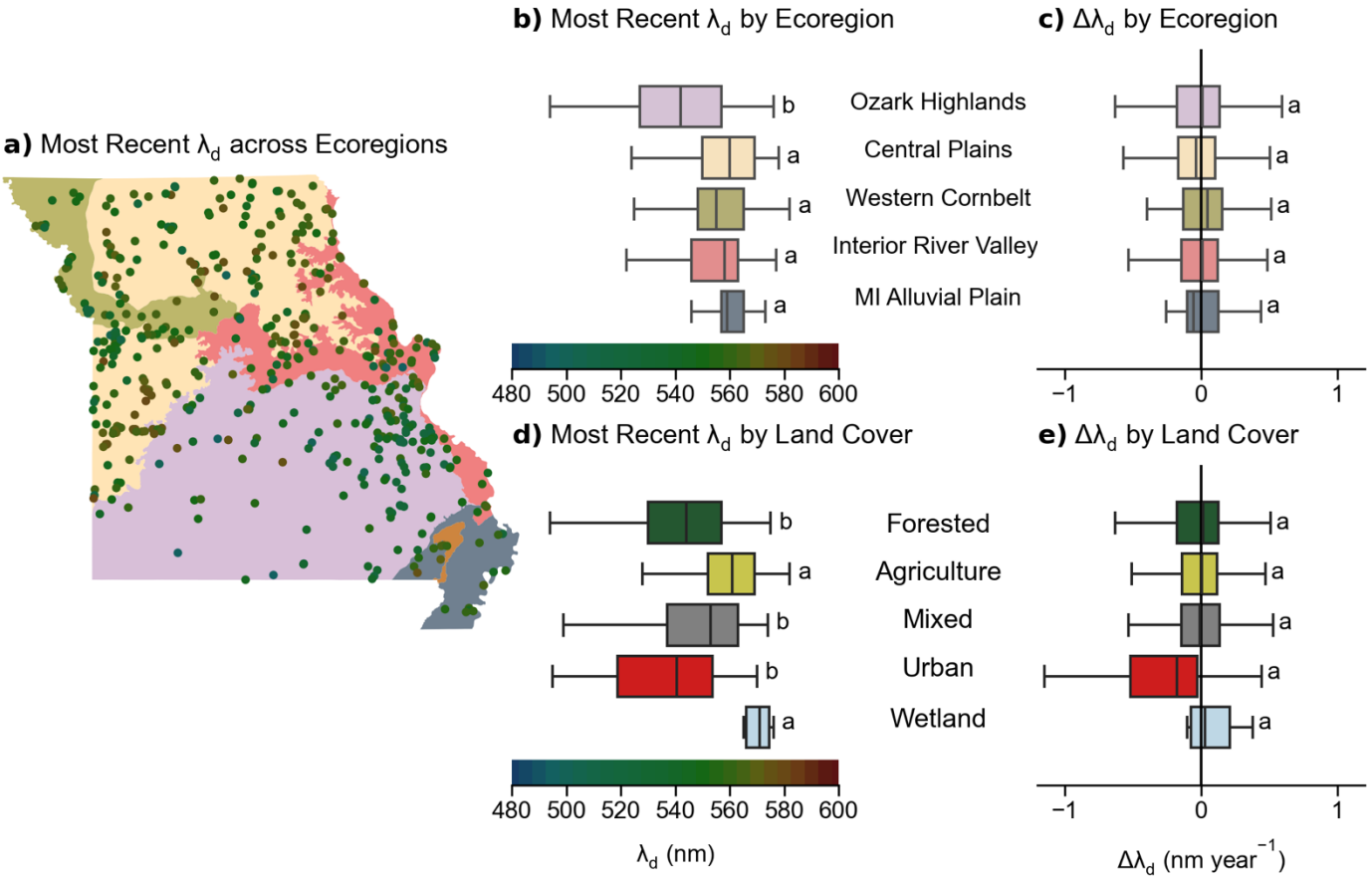

752

753 **Figure 5**

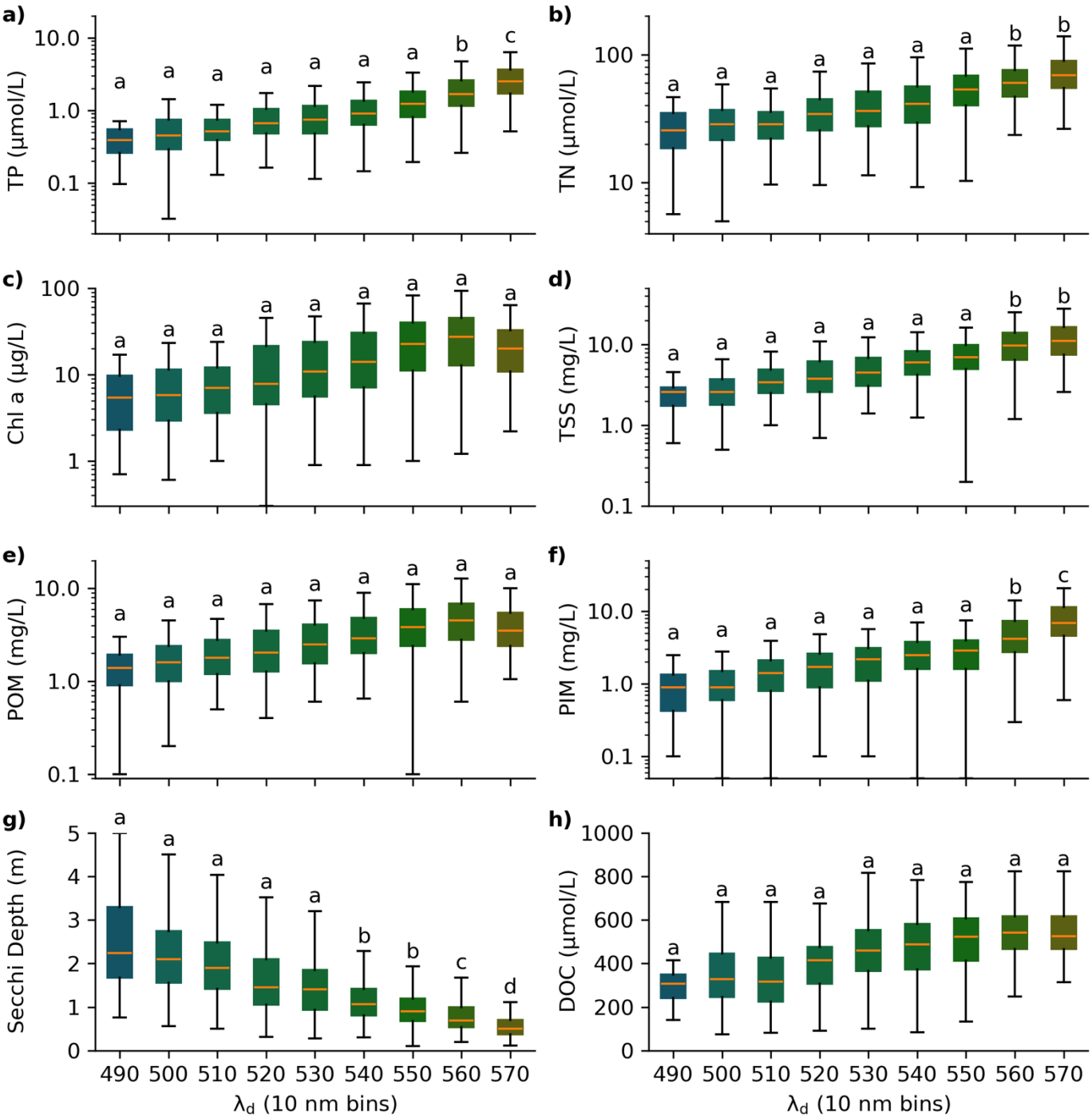

754

Figure 6

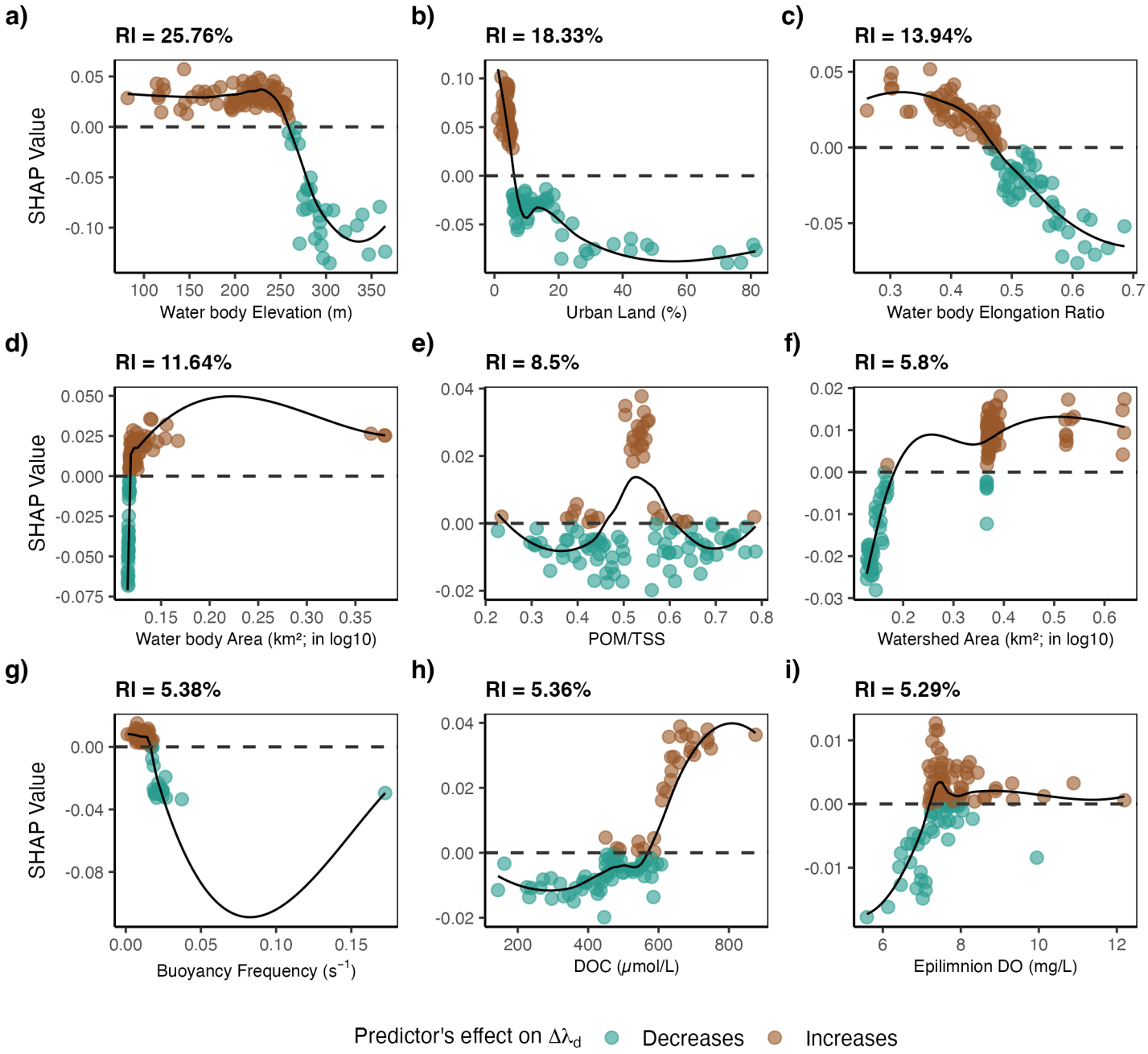
a)
RI = 25.76%
SHAP Value
Water body Elevation (m)
b)
RI = 18.33%
Urban Land (%)
c)
RI = 13.94%
Water body Elongation Ratio
d)
RI = 11.64%
Water body Area (km²; in log10)
e)
RI = 8.5%
POM/TSS
f)
RI = 5.8%
Watershed Area (km²; in log10)
g)
RI = 5.38%
Buoyancy Frequency (s⁻¹)
h)
RI = 5.36%
DOC (μmol/L)
i)
RI = 5.29%
Epilimnion DO (mg/L)
Predictor's effect on Δλd
Decreases
Increases

Supplementary Material

Table S1. List of libraries and functions used for the statistical analyses employed in the study.

Analysis	Software	Libraries	Function	Reference
Geospatial analysis	Python	PySheds		Bartos, 2020
		geopandas		Van den Bossche et al., 2024
		shapely		Gillies et al., 2022
		numpy		Harris et al., 2020
Brunt-Väisälä buoyancy frequency	R	RLakeAnalyzer		Winslow et al., 2019
Linear mixed-effects models	R	lmerTest		Kuznetsova et al., 2017
		parameters		Lüdecke et al., 2020
		lme4	*lmer*	Bates et al., 2015
		MuMIn	*r.squaredGLMM*	Bartoń, 2024
Trend analysis	R	trend	*sens.slope*	Pohlert, 2020
			mk.test	
Boosted Regression Trees	R	dismo	*gbm.step*	Hijmans et al., 2023
		gbm		Greenwell et al., 2022
Shapley	R	iml		Molnar et al., 2018

Table S2. Instrumentation used for the analysis of water quality parameters in this study (Jones et al., 2024a, 2024b; North et al., 2025).

Parameter	Years	Instrument	Resolution	Accuracy	MDL	Filter Pore Size	Method
Water Temperature	<2000 2000-2006 2007-2016 2017-2020	YSI 50B YSI 85 YSI 550A YSI EXO3	0.1°C 0.1°C 0.1°C 0.001°C	± 0.1°C ± 0.1°C ± 0.2°C ± 0.01°C	-	unfiltered	Multiparameter sensor
Dissolved Oxygen	<2000 2000-2006 2007-2016 2017-2020	YSI 50B YSI 85 YSI 550A YSI EXO3	0.01 mg/L	± 0.3 mg/L ± 0.3 mg/L ± 0.3 mg/L ± 0.1 mg/L	-	unfiltered	Multiparameter sensor.
Total (uncorrected) Chlorophyll	< 2018 2019- 2020	Turner Designs TD-700 Fluorometer Cary Eclipse Fluorometer	-	-	0.30 µg/L 0.30 µg/L 0.70 µg/L	1.0 µm, Pall A/E glass fiber filter 0.7 µm GFF 0.7 µm GFF	Fluorometric analysis following U.S. Environmental Protection Agency method 445.0 (Arar and Collins, 1997), modified using heated ethanol extraction without homogenization (Sartory and Grobbelaar, 1984) and a fluorometer equipped with a flow-through cell (Knowlton, 1984).
Total Nitrogen	<2020	Genysis 2 Spectrophotometer	-	-	2.500 µmol N/L	unfiltered	Second derivative spectroscopy (Crumpton et al. 1992) following persulfate digestion (APHA, Standard Methods For the Examination of Water and Wastewater (23rd ed). 2017. Method num. 4500-N. C. Nitrogen. DOI: 10.2105/SMWW.2882.086.
Total Phosphorus	<2020	Genysis 2 Spectrophotometer	-	-	0.032 µmol P/L	unfiltered	Spectrophotometry, persulfate digestion, and ascorbic acid method; APHA, Standard Methods For the Examination of Water and Wastewater (23rd ed). 2017. Method num. 4500-P.B.5.E. Phosphorus. DOI: 10.2105/SMWW.2882.093.

Total Suspended Solids	<2020	Mettler Toledo model AB54 analytical balance	-	-	0.1 mg/L	1.5 um Whatman glass microfiber filters, Grade 934-AH	APHA, Standard Methods For the Examination of Water and Wastewater (23rd ed). 2017. Method num. 2540D. Solids. DOI: 10.2105/SMWW.2882.030.
Particulate Organic Matter							
Particulate Inorganic Matter							
Dissolved Organic Carbon	<2020	Shimadzu TOC-VCPH Analyzer	-	-	0.2 mg/L	1.5 um Whatman glass microfiber filters, Grade 934-AH	High-temperature combustion method; APHA, Standard Methods For the Examination of Water and Wastewater (23rd ed). 2017. Method num. 5310B. Total organic carbon. DOI: 10.2105/SMWW.2882.104
Secchi Depth	<2020	20 cm black/white disk	-	-	0.10 m	unfiltered	-

Table S3. List of references for the statistical analyses employed in the study.

Statistical analysis	Reference
Linear mixed-effects models	Laird and Ware, 1982
Sen's slope test	Sen, 1968
Mann-Kendall trend test	Mann, 1945
	Kendall, 1975

Table S4. Results of boosted regression trees (BRT), including performance metrics for both training and cross-validated data. Models with missing values are included in the table and reflect cases where convergence was not achieved due to large learning rates or step sizes. Model highlighted in bold is the selected model.

Model	Setting	Training Data				Cross-Validated Data	
		Mean Total Deviance	Mean Residual Deviance	Correlation	R^2	Estimated Deviance	Correlation
Model 1	lr=0.05, tc=1, bg=0.5	-	-	-	-	-	-
Model 2	lr=0.01, tc=1, bg=0.5	-	-	-	-	-	-
Model 3	lr=0.005, tc=1, bg=0.5	0.11	0.08	0.66	32.40	0.11	0.24
Model 4	lr=0.001, tc=1, bg=0.5	0.11	0.08	0.67	33.70	0.11	0.25
Model 5	lr=0.0005, tc=1, bg=0.5	0.11	0.08	0.65	27.90	0.11	0.24
Model 6	lr=0.05, tc=5, bg=0.5	-	-	-	-	-	-
Model 7	lr=0.01, tc=5, bg=0.5	-	-	-	-	-	-
Model 8	lr=0.005, tc=5, bg=0.5	0.11	0.07	0.77	40.40	0.11	0.27
Model 9	lr=0.001, tc=5, bg=0.5	0.11	0.06	0.80	46.00	0.11	0.30
Model 10	lr=0.0005, tc=5, bg=0.5	0.11	0.06	0.80	45.60	0.11	0.20
Model 11	lr=0.05, tc-10, bg=0.5	-	-	-	-	-	-
Model 12	lr=0.01, tc=10, bg=0.5	-	-	-	-	-	-
Model 13	lr=0.005, tc=10, bg=0.5	0.11	0.07	0.76	34.90	0.11	0.32
Model 14	lr=0.001, tc=10, bg=0.5	0.11	0.07	0.76	35.40	0.11	0.19
Model 15	lr=0.0005, tc=10, bg=0.5	0.11	0.07	0.78	40.00	0.11	0.27
Model 16	lr=0.05, tc=1, bg=0.75	-	-	-	-	-	-
Model 17	lr=0.01, tc=1, bg=0.75	-	-	-	-	-	-
Model 18	lr=0.005, tc=1, bg=0.75	0.11	0.08	0.67	30.80	0.11	0.18
Model 19	lr=0.001, tc=1, bg=0.75	0.11	0.07	0.70	35.90	0.11	0.20
Model 20	lr=0.0005, tc=1, bg=0.75	0.11	0.08	0.68	33.60	0.11	0.28
Model 21	lr=0.05, tc=5, bg=0.75	-	-	-	-	-	-
Model 22	lr=0.01, tc=5, bg=0.75	-	-	-	-	-	-
Model 23	lr=0.001, tc=5, bg=0.75	0.11	0.06	0.86	49.90	0.11	0.28
Model 24	lr=0.001, tc=5, bg=0.75	0.11	0.08	0.82	30.20	0.11	0.15
Model 25	**lr=0.0005, tc=5, bg=0.75**	**0.11**	**0.06**	**0.87**	**51.70**	**0.11**	**0.25**
Model 26	lr=0.05, tc=10, bg=0.75	-	-	-	-	-	-
Model 27	lr=0.01, tc=10, bg=0.75	0.11	0.04	0.90	65.6	0.10	0.30
Model 28	lr=0.005, tc=10, bg=0.75	-	-	-	-	-	-
Model 29	lr=0.001, tc=10, bg=0.75	-	-	-	-	-	-
Model 30	lr=0.0005, tc=10, bg=0.75	0.11	0.05	0.89	60.00	0.11	0.25

Table S5. Number of observations (*n*), mean, standard deviation (SD), minimum, and maximum of reservoir catchment characteristics in Missouri.

Ecoregion	Waterbody elevation (m)	Waterbody area (Km^2)	Waterbody elongation ratio	Watershed area (Km^2)	Watershed elongation ratio	Warea/ Rarea
Ozark Highlands						
n	66	66	66	66	66	66
Mean	232	21.138	0.47	692.73	0.69	136
SD	74	69.395	0.13	1606.03	0.09	417
Minimum	70	0.003	0.16	0.02	0.49	3
Maximum	438	335.495	0.72	7049.67	0.95	3001
Central Irregular Plains						
n	150	150	150	150	150	150
Mean	249	1.076	0.50	27.49	0.68	33
SD	30	2.955	0.10	83.73	0.09	76
Minimum	168	0.004	0.27	0.03	0.35	1
Maximum	318	27.412	0.79	611.22	0.84	883
Western Corn Belt Plains						
n	20	20	20	20	20	20
Mean	262.	3.531	0.47	60.03	0.68	33
SD	35	11.652	0.12	196.10	0.09	41
Minimum	208	0.008	0.23	0.09	0.43	4
Maximum	32	52.598	0.64	887.97	0.81	135
Interior River Valleys and Hills						
n	60	60	60	60	60	60
Mean	187	2.754	0.51	184.06	0.67	110
SD	38	17.715	0.10	1271.22	0.10	524
Minimum	116	0.003	0.29	0.05	0.42	3
Maximum	303	137.612	0.79	9861.20	0.89	4063
Mississippi Alluvial Plain						
n	2	2	2	2	2	2
Mean	80	0.419	0.72	39.51	0.64	64
SD	18	0.302	0.38	54.65	0.18	84
Minimum	67	0.206	0.46	0.87	0.52	4
Maximum	92	0.633	0.99	78.15	0.76	123

Table S6. Number of observations (*n*), mean, standard deviation (SD), minimum, and maximum of biochemical parameters in Missouri reservoirs.

Ecoregion	Chla-*a* (µg/L)	Secchi depth (m)	TN (µmol N/L)	TP (µmol P/L)	TN/TP (in log)	DOC (µmol/L)	POM (mg/L)	PIM (mg/L)	TSS (mg/L)	POM/TSS	PIM/TSS	Epilimnion DO (mg/L)	Hypolimnion DO (mg/L)
Ozark Highlands													
n	66	66	66	66	66	55	64	65	64	64	64	57	57
Mean	9.79	1.76	37.352	0.918	3.858	363.3	2.1	3.0	5.0	0.5	0.5	7.90	2.49
SD	16.87	0.91	23.344	0.967	0.513	134.3	2.3	4.5	5.5	0.2	0.2	1.62	2.66
Minimum	1.00	0.45	7.138	0.204	2.690	83.9	0.3	0.2	0.8	0.1	0.1	3.03	0.00
Maximum	121.50	4.17	112.063	6.135	5.102	707.7	15.6	26.6	30.7	0.9	0.9	12.20	8.97
Central Irregular Plains													
n	150	150	150	150	150	121	150	150	150	150	150	126	126
Mean	24.03	0.98	69.150	2.248	3.584	542.8	4.6	9.6	14.1	0.5	0.5	7.83	1.44
SD	29.05	0.71	42.815	2.178	0.527	106.6	4.1	18.2	21.2	0.2	0.2	2.07	2.12
Minimum	0.60	0.10	28.551	0.226	2.256	278.9	0.6	0.1	1.6	0.1	0.0	3.40	0.00
Maximum	237.70	4.50	299.072	18.986	5.024	899.3	23.5	119.7	138.5	1.0	0.9	15.70	10.30
Western Corn Belt Plains													
n	20	20	20	20	20	13	20	20	20	20	20	14	14
Mean	47.48	1.33	82.138	2.782	3.669	477.5	8.7	9.7	18.4	0.5	0.5	8.73	0.57
SD	80.38	0.94	85.724	4.723	0.559	107.1	16.3	23.2	37.6	0.2	0.2	3.15	0.81
Minimum	2.00	0.10	18.558	0.226	2.759	352.0	1.3	0.9	2.8	0.1	0.2	4.83	0.00
Maximum	323.20	3.60	361.884	20.407	4.964	742.3	61.4	107.0	168.4	0.8	0.9	14.70	3.00
Interior River Valleys and Hills													
n	60	59	60	60	60	28	60	60	60	60	60	32	32
Mean	21.18	1.32	56.379	1.837	3.734	512.7	4.2	7.4	11.6	0.5	0.5	7.37	1.52
SD	33.91	1.07	31.883	2.060	0.665	143.4	4.7	20.5	24.1	0.2	0.2	2.74	2.22
Minimum	0.70	0.10	17.131	0.242	2.186	291.4	0.2	0.1	0.7	0.1	0.0	3.71	0.00

Maximum	168.40	6.76	201.285	10.655	5.015	918.7	26.7	151.2	177.9	1.0	0.9	16.30	9.00
Mississippi Alluvial Plain													
n	2	2	2	2	2	0	2	2	2	2	2	1	1
Mean	125.10	0.52	81.370	3.826	3.237	-	11.7	3.3	15.0	0.8	0.2	10.80	4.50
SD	173.52	0.33	82.773	4.407	0.330	-	14.8	4.3	19.2	0.1	0.1	-	-
Minimum	2.40	0.28	22.841	0.710	3.003	-	1.2	0.2	1.4	0.8	0.1	10.80	4.50
Maximum	247.80	0.75	139.900	6.942	3.471	-	22.2	6.3	28.5	0.9	0.2	10.80	4.50

Table S7. Number of reservoirs (*n*), mean, standard deviation (SD), minimum, and maximum of physical parameters in Missouri reservoirs.

Ecoregion	Surface wtemp (℃)	Buoyancy frequency (s^{-2})	Thermocline depth (m)	Hypolimnion wtemp (℃)	Oxycline (m)	Hypoxycline (m)
Ozark Highlands						
n	58	58	58	58	58	54
Mean	24.1	0.013	3.6	14.3	3.1	5.6
SD	3.3	0.018	1.6	5.5	2.2	2.8
Minimum	16.8	0.002	0.3	7.9	0.1	2.0
Maximum	35.0	0.126	7.5	31.5	9.5	12.0
Central Irregular Plains						
n	126	126	126	126	126	126
Mean	25.1	0.010	2.9	16.8	2.0	3.7
SD	4.4	0.007	1.4	4.5	1.2	1.4
Minimum	15.4	0.000	0.1	7.1	0.1	0.5
Maximum	33.4	0.044	6.5	31.8	7.5	8.0
Western Corn Belt Plains						
n	15	15	14	14	15	14
Mean	25.2	0.008	3.9	15.7	2.3	4.5
SD	2.6	0.004	2.2	3.7	1.0	1.6
Minimum	21.8	0.001	0.8	8.0	0.8	2.0
Maximum	30.9	0.016	8.5	23.1	4.5	8.0
Interior River Valleys and Hills						
n	32	32	32	32	32	32
Mean	23.1	0.013	3.1	13.4	2.8	4.1
SD	4.1	0.019	1.2	5.2	1.7	1.6
Minimum	17.0	0.000	0.1	6.3	0.5	1.5
Maximum	29.4	0.111	5.5	24.2	8.3	9.5
Mississippi Alluvial Plain						
n	1	1	1	1	1	0
Mean	25.8	0.005	0.8	24.4	0.8	-
SD	-	-	-	-	-	-
Minimum	25.8	0.005	0.8	24.4	0.8	-
Maximum	25.8	0.005	0.8	24.4	0.8	-

Table S8. List of reservoirs (n = 478) with corresponding identification (Hylak_id and MULakeNumber) and associated ecoregion. NA in MULakeNumber column indicates reservoirs that have Hylak_id and are included in the LimnoSat dataset but are not monitored the water quality programs.

Hylak_id	MULakeNumber	Ecoregion
9207	46	Central Irregular Plains
9219	72	Central Irregular Plains
112053	51	Central Irregular Plains
112111	131	Central Irregular Plains
112141	133	Central Irregular Plains
112187	80	Central Irregular Plains
112214	178	Central Irregular Plains
112254	NA	Central Irregular Plains
112259	45	Central Irregular Plains
112285	47	Central Irregular Plains
112389	148	Central Irregular Plains
112394	116	Central Irregular Plains
112403	67	Central Irregular Plains
112406	68	Central Irregular Plains
112425	69	Central Irregular Plains
112429	157	Central Irregular Plains
112488	90	Central Irregular Plains
112556	NA	Central Irregular Plains
112557	91	Central Irregular Plains
1055455	NA	Central Irregular Plains
1055511	NA	Central Irregular Plains
1055519	132	Central Irregular Plains
1055538	182	Central Irregular Plains
1055550	85	Central Irregular Plains
1055553	NA	Central Irregular Plains
1055589	53	Central Irregular Plains
1055598	141	Central Irregular Plains
1055615	NA	Central Irregular Plains
1055620	NA	Central Irregular Plains
1055622	NA	Central Irregular Plains
1055628	84	Central Irregular Plains
1055629	185	Central Irregular Plains

1055635	NA	Central Irregular Plains
1055644	NA	Central Irregular Plains
1055652	NA	Central Irregular Plains
1055653	NA	Central Irregular Plains
1055700	NA	Central Irregular Plains
1055707	83	Central Irregular Plains
1055719	NA	Central Irregular Plains
1055721	NA	Central Irregular Plains
1055738	NA	Central Irregular Plains
1055740	137	Central Irregular Plains
1055742	NA	Central Irregular Plains
1055761	55	Central Irregular Plains
1055764	NA	Central Irregular Plains
1055770	164	Central Irregular Plains
1055796	86	Central Irregular Plains
1055801	56	Central Irregular Plains
1055822	57	Central Irregular Plains
1055913	NA	Central Irregular Plains
1055923	50	Central Irregular Plains
1055931	NA	Central Irregular Plains
1055932	NA	Central Irregular Plains
1055940	129	Central Irregular Plains
1055949	NA	Central Irregular Plains
1055955	NA	Central Irregular Plains
1055956	NA	Central Irregular Plains
1055977	NA	Central Irregular Plains
1056004	NA	Central Irregular Plains
1056005	222	Central Irregular Plains
1056008	163	Central Irregular Plains
1056011	NA	Central Irregular Plains
1056012	130	Central Irregular Plains
1056018	114	Central Irregular Plains
1056073	NA	Central Irregular Plains
1056107	NA	Central Irregular Plains
1056123	191	Central Irregular Plains
1056147	82	Central Irregular Plains
1056153	NA	Central Irregular Plains
1056185	NA	Central Irregular Plains
1056210	NA	Central Irregular Plains
1056231	317	Central Irregular Plains

1056241	123	Central Irregular Plains
1056245	81	Central Irregular Plains
1056258	87	Central Irregular Plains
1056261	NA	Central Irregular Plains
1056264	NA	Central Irregular Plains
1056285	213	Central Irregular Plains
1056296	211	Central Irregular Plains
1056312	49	Central Irregular Plains
1056317	78	Central Irregular Plains
1056341	59	Central Irregular Plains
1056344	139	Central Irregular Plains
1056349	NA	Central Irregular Plains
1056359	115	Central Irregular Plains
1056376	NA	Central Irregular Plains
1056378	NA	Central Irregular Plains
1056409	NA	Central Irregular Plains
1056415	88	Central Irregular Plains
1056462	NA	Central Irregular Plains
1056479	NA	Central Irregular Plains
1056505	NA	Central Irregular Plains
1056506	NA	Central Irregular Plains
1056538	NA	Central Irregular Plains
1056542	NA	Central Irregular Plains
1056545	NA	Central Irregular Plains
1056563	NA	Central Irregular Plains
1056569	NA	Central Irregular Plains
1056612	NA	Central Irregular Plains
1056706	NA	Central Irregular Plains
1056724	74	Central Irregular Plains
1056766	286	Central Irregular Plains
1056947	NA	Central Irregular Plains
1056969	NA	Central Irregular Plains
1056992	NA	Central Irregular Plains
1057006	NA	Central Irregular Plains
1057019	NA	Central Irregular Plains
1057022	NA	Central Irregular Plains
1057023	299	Central Irregular Plains
1057087	NA	Central Irregular Plains
1057090	NA	Central Irregular Plains
1057104	41	Central Irregular Plains

1057123	NA	Central Irregular Plains
1057133	NA	Central Irregular Plains
1057140	NA	Central Irregular Plains
1057184	65	Central Irregular Plains
1057216	NA	Central Irregular Plains
1057220	NA	Central Irregular Plains
1057230	NA	Central Irregular Plains
1057242	64	Central Irregular Plains
1057248	NA	Central Irregular Plains
1057267	NA	Central Irregular Plains
1057277	66	Central Irregular Plains
1057287	113	Central Irregular Plains
1057292	NA	Central Irregular Plains
1057311	NA	Central Irregular Plains
1057315	NA	Central Irregular Plains
1057319	NA	Central Irregular Plains
1057321	NA	Central Irregular Plains
1057328	NA	Central Irregular Plains
1057329	NA	Central Irregular Plains
1057331	117	Central Irregular Plains
1057343	NA	Central Irregular Plains
1057344	241	Central Irregular Plains
1057351	166	Central Irregular Plains
1057352	165	Central Irregular Plains
1057369	169	Central Irregular Plains
1057396	183	Central Irregular Plains
1057406	118	Central Irregular Plains
1057408	NA	Central Irregular Plains
1057418	NA	Central Irregular Plains
1057419	NA	Central Irregular Plains
1057422	120	Central Irregular Plains
1057442	NA	Central Irregular Plains
1057517	NA	Central Irregular Plains
1057521	NA	Central Irregular Plains
1057539	70	Central Irregular Plains
1057575	NA	Central Irregular Plains
1057611	62	Central Irregular Plains
1057641	63	Central Irregular Plains
1057662	NA	Central Irregular Plains
1057680	266	Central Irregular Plains

1057688	NA	Central Irregular Plains
1057700	NA	Central Irregular Plains
1057727	NA	Central Irregular Plains
1057743	265	Central Irregular Plains
1057777	NA	Central Irregular Plains
1057786	NA	Central Irregular Plains
1057808	NA	Central Irregular Plains
1057812	NA	Central Irregular Plains
1057819	NA	Central Irregular Plains
1057854	261	Central Irregular Plains
1057857	NA	Central Irregular Plains
1057870	NA	Central Irregular Plains
1057914	NA	Central Irregular Plains
1057928	NA	Central Irregular Plains
1057959	189	Central Irregular Plains
1058026	NA	Central Irregular Plains
1058110	NA	Central Irregular Plains
1058258	NA	Central Irregular Plains
1058269	159	Central Irregular Plains
1058283	NA	Central Irregular Plains
1058300	NA	Central Irregular Plains
1058322	NA	Central Irregular Plains
1058332	NA	Central Irregular Plains
1058341	NA	Central Irregular Plains
1058350	NA	Central Irregular Plains
1058354	160	Central Irregular Plains
1058361	NA	Central Irregular Plains
1058365	NA	Central Irregular Plains
1058366	NA	Central Irregular Plains
1058381	NA	Central Irregular Plains
1058383	NA	Central Irregular Plains
1058393	NA	Central Irregular Plains
1058506	NA	Central Irregular Plains
1058512	NA	Central Irregular Plains
1058514	NA	Central Irregular Plains
1058528	NA	Central Irregular Plains
1058659	NA	Central Irregular Plains
1058711	161	Central Irregular Plains
1058915	NA	Central Irregular Plains
1058918	94	Central Irregular Plains

1058962	NA	Central Irregular Plains
1058982	NA	Central Irregular Plains
1059038	NA	Central Irregular Plains
1059070	NA	Central Irregular Plains
112172	58	Interior River Valleys and Hills
112421	6	Interior River Valleys and Hills
112432	9	Interior River Valleys and Hills
112628	NA	Interior River Valleys and Hills
1055777	NA	Interior River Valleys and Hills
1056084	NA	Interior River Valleys and Hills
1056088	NA	Interior River Valleys and Hills
1056274	NA	Interior River Valleys and Hills
1056293	NA	Interior River Valleys and Hills
1056469	60	Interior River Valleys and Hills
1056486	238	Interior River Valleys and Hills
1056541	NA	Interior River Valleys and Hills
1056591	NA	Interior River Valleys and Hills
1056593	NA	Interior River Valleys and Hills
1056613	NA	Interior River Valleys and Hills
1056684	272	Interior River Valleys and Hills
1056777	NA	Interior River Valleys and Hills
1057007	44	Interior River Valleys and Hills
1057018	43	Interior River Valleys and Hills
1057027	NA	Interior River Valleys and Hills
1057076	NA	Interior River Valleys and Hills
1057126	NA	Interior River Valleys and Hills
1057183	5	Interior River Valleys and Hills
1057266	NA	Interior River Valleys and Hills
1057273	NA	Interior River Valleys and Hills
1057275	NA	Interior River Valleys and Hills
1057330	NA	Interior River Valleys and Hills
1057341	NA	Interior River Valleys and Hills
1057342	NA	Interior River Valleys and Hills
1057347	NA	Interior River Valleys and Hills
1057380	NA	Interior River Valleys and Hills
1057382	NA	Interior River Valleys and Hills
1057388	NA	Interior River Valleys and Hills
1057410	NA	Interior River Valleys and Hills
1057411	2	Interior River Valleys and Hills
1057421	NA	Interior River Valleys and Hills

1057440	298	Interior River Valleys and Hills
1057441	NA	Interior River Valleys and Hills
1057444	NA	Interior River Valleys and Hills
1057455	NA	Interior River Valleys and Hills
1057463	293	Interior River Valleys and Hills
1057467	274	Interior River Valleys and Hills
1057472	NA	Interior River Valleys and Hills
1057475	NA	Interior River Valleys and Hills
1057480	277	Interior River Valleys and Hills
1057483	NA	Interior River Valleys and Hills
1057497	NA	Interior River Valleys and Hills
1057503	7	Interior River Valleys and Hills
1057513	NA	Interior River Valleys and Hills
1057519	NA	Interior River Valleys and Hills
1057529	403	Interior River Valleys and Hills
1057545	NA	Interior River Valleys and Hills
1057546	442	Interior River Valleys and Hills
1057549	NA	Interior River Valleys and Hills
1057560	280	Interior River Valleys and Hills
1057564	NA	Interior River Valleys and Hills
1057567	NA	Interior River Valleys and Hills
1057577	NA	Interior River Valleys and Hills
1057581	NA	Interior River Valleys and Hills
1057619	13	Interior River Valleys and Hills
1057657	NA	Interior River Valleys and Hills
1057671	NA	Interior River Valleys and Hills
1057783	NA	Interior River Valleys and Hills
1058314	NA	Interior River Valleys and Hills
1058452	NA	Interior River Valleys and Hills
1058544	NA	Interior River Valleys and Hills
1058660	25	Interior River Valleys and Hills
1058926	26	Interior River Valleys and Hills
1059243	29	Interior River Valleys and Hills
1059163	NA	Mississippi Alluvial Plain
1059175	NA	Mississippi Alluvial Plain
1059438	NA	Mississippi Alluvial Plain
1059445	201	Mississippi Alluvial Plain
1059500	NA	Mississippi Alluvial Plain
1059519	NA	Mississippi Alluvial Plain
1059528	NA	Mississippi Alluvial Plain

1059550	NA	Mississippi Alluvial Plain
1059599	NA	Mississippi Alluvial Plain
1059604	NA	Mississippi Alluvial Plain
1059637	NA	Mississippi Alluvial Plain
1059652	NA	Mississippi Alluvial Plain
1059654	NA	Mississippi Alluvial Plain
1059661	NA	Mississippi Alluvial Plain
1059719	NA	Mississippi Alluvial Plain
1059722	NA	Mississippi Alluvial Plain
1059848	NA	Mississippi Alluvial Plain
1059854	NA	Mississippi Alluvial Plain
1059860	NA	Mississippi Alluvial Plain
1059865	NA	Mississippi Alluvial Plain
1059870	NA	Mississippi Alluvial Plain
1059530	NA	Mississippi Valley Loess Plains
804	NA	Ozark Highlands
808	100	Ozark Highlands
9268	92	Ozark Highlands
9322	101	Ozark Highlands
112542	111	Ozark Highlands
112563	21	Ozark Highlands
112606	39	Ozark Highlands
112627	NA	Ozark Highlands
112679	96	Ozark Highlands
112722	36	Ozark Highlands
1057625	184	Ozark Highlands
1057640	12	Ozark Highlands
1057651	306	Ozark Highlands
1057666	NA	Ozark Highlands
1057702	NA	Ozark Highlands
1057703	NA	Ozark Highlands
1057711	NA	Ozark Highlands
1057715	NA	Ozark Highlands
1057725	420	Ozark Highlands
1057726	NA	Ozark Highlands
1057730	NA	Ozark Highlands
1057736	NA	Ozark Highlands
1057750	NA	Ozark Highlands
1057756	NA	Ozark Highlands
1057772	NA	Ozark Highlands

1057773	NA	Ozark Highlands
1057774	NA	Ozark Highlands
1057787	10	Ozark Highlands
1057809	NA	Ozark Highlands
1057880	11	Ozark Highlands
1057889	NA	Ozark Highlands
1057894	NA	Ozark Highlands
1057916	NA	Ozark Highlands
1057926	NA	Ozark Highlands
1057931	14	Ozark Highlands
1057962	NA	Ozark Highlands
1057966	NA	Ozark Highlands
1057974	NA	Ozark Highlands
1057995	NA	Ozark Highlands
1058002	NA	Ozark Highlands
1058017	NA	Ozark Highlands
1058019	15	Ozark Highlands
1058022	NA	Ozark Highlands
1058023	NA	Ozark Highlands
1058044	NA	Ozark Highlands
1058064	NA	Ozark Highlands
1058076	310	Ozark Highlands
1058083	NA	Ozark Highlands
1058118	NA	Ozark Highlands
1058136	NA	Ozark Highlands
1058143	NA	Ozark Highlands
1058173	NA	Ozark Highlands
1058196	NA	Ozark Highlands
1058201	NA	Ozark Highlands
1058225	NA	Ozark Highlands
1058228	NA	Ozark Highlands
1058248	NA	Ozark Highlands
1058252	NA	Ozark Highlands
1058263	NA	Ozark Highlands
1058264	NA	Ozark Highlands
1058306	NA	Ozark Highlands
1058317	NA	Ozark Highlands
1058342	NA	Ozark Highlands
1058343	NA	Ozark Highlands
1058351	NA	Ozark Highlands

1058359	NA	Ozark Highlands
1058375	110	Ozark Highlands
1058377	NA	Ozark Highlands
1058380	NA	Ozark Highlands
1058388	NA	Ozark Highlands
1058396	NA	Ozark Highlands
1058418	NA	Ozark Highlands
1058419	NA	Ozark Highlands
1058424	22	Ozark Highlands
1058426	40	Ozark Highlands
1058436	NA	Ozark Highlands
1058440	NA	Ozark Highlands
1058443	NA	Ozark Highlands
1058446	23	Ozark Highlands
1058455	NA	Ozark Highlands
1058456	267	Ozark Highlands
1058457	NA	Ozark Highlands
1058465	17	Ozark Highlands
1058466	NA	Ozark Highlands
1058478	NA	Ozark Highlands
1058489	18	Ozark Highlands
1058490	112	Ozark Highlands
1058492	NA	Ozark Highlands
1058493	19	Ozark Highlands
1058494	152	Ozark Highlands
1058496	263	Ozark Highlands
1058498	NA	Ozark Highlands
1058529	NA	Ozark Highlands
1058534	NA	Ozark Highlands
1058542	NA	Ozark Highlands
1058556	271	Ozark Highlands
1058560	NA	Ozark Highlands
1058579	NA	Ozark Highlands
1058613	NA	Ozark Highlands
1058630	NA	Ozark Highlands
1058651	NA	Ozark Highlands
1058652	186	Ozark Highlands
1058657	NA	Ozark Highlands
1058679	NA	Ozark Highlands
1058685	NA	Ozark Highlands

1058686	NA	Ozark Highlands
1058699	NA	Ozark Highlands
1058707	NA	Ozark Highlands
1058720	NA	Ozark Highlands
1058745	NA	Ozark Highlands
1058751	NA	Ozark Highlands
1058752	107	Ozark Highlands
1058756	NA	Ozark Highlands
1058761	NA	Ozark Highlands
1058764	268	Ozark Highlands
1058810	38	Ozark Highlands
1058822	24	Ozark Highlands
1058866	NA	Ozark Highlands
1058867	NA	Ozark Highlands
1058895	37	Ozark Highlands
1058899	NA	Ozark Highlands
1058943	NA	Ozark Highlands
1058980	146	Ozark Highlands
1059042	NA	Ozark Highlands
1059074	NA	Ozark Highlands
1059103	95	Ozark Highlands
1059122	28	Ozark Highlands
1059132	NA	Ozark Highlands
1059151	NA	Ozark Highlands
1059156	NA	Ozark Highlands
1059174	NA	Ozark Highlands
1059188	NA	Ozark Highlands
1059253	NA	Ozark Highlands
1059271	NA	Ozark Highlands
1059301	NA	Ozark Highlands
1059306	NA	Ozark Highlands
1059311	NA	Ozark Highlands
1059328	97	Ozark Highlands
1059392	NA	Ozark Highlands
1059402	104	Ozark Highlands
1059433	NA	Ozark Highlands
1059553	NA	Ozark Highlands
1059554	NA	Ozark Highlands
1059628	NA	Ozark Highlands
1059629	NA	Ozark Highlands

1059636	33	Ozark Highlands
1059650	NA	Ozark Highlands
1059674	NA	Ozark Highlands
1059683	NA	Ozark Highlands
112102	181	Western Corn Belt Plains
112162	NA	Western Corn Belt Plains
112163	NA	Western Corn Belt Plains
112221	NA	Western Corn Belt Plains
112225	76	Western Corn Belt Plains
112250	NA	Western Corn Belt Plains
112269	75	Western Corn Belt Plains
112284	NA	Western Corn Belt Plains
112321	NA	Western Corn Belt Plains
112362	NA	Western Corn Belt Plains
1055604	179	Western Corn Belt Plains
1055671	180	Western Corn Belt Plains
1055692	NA	Western Corn Belt Plains
1055915	NA	Western Corn Belt Plains
1055930	NA	Western Corn Belt Plains
1056283	NA	Western Corn Belt Plains
1056397	NA	Western Corn Belt Plains
1056417	NA	Western Corn Belt Plains
1056560	NA	Western Corn Belt Plains
1056581	NA	Western Corn Belt Plains
1056643	NA	Western Corn Belt Plains
1056803	NA	Western Corn Belt Plains
1056837	NA	Western Corn Belt Plains
1056843	NA	Western Corn Belt Plains
1056932	155	Western Corn Belt Plains
1056933	71	Western Corn Belt Plains
1056943	NA	Western Corn Belt Plains
1056965	406	Western Corn Belt Plains
1056973	NA	Western Corn Belt Plains
1056976	NA	Western Corn Belt Plains
1056984	NA	Western Corn Belt Plains
1056988	NA	Western Corn Belt Plains
1057080	NA	Western Corn Belt Plains
1057132	121	Western Corn Belt Plains
1057151	NA	Western Corn Belt Plains
1057168	150	Western Corn Belt Plains

1057178	NA	Western Corn Belt Plains
1057192	NA	Western Corn Belt Plains
1057221	162	Western Corn Belt Plains
1057226	NA	Western Corn Belt Plains
1057227	NA	Western Corn Belt Plains
1057274	NA	Western Corn Belt Plains

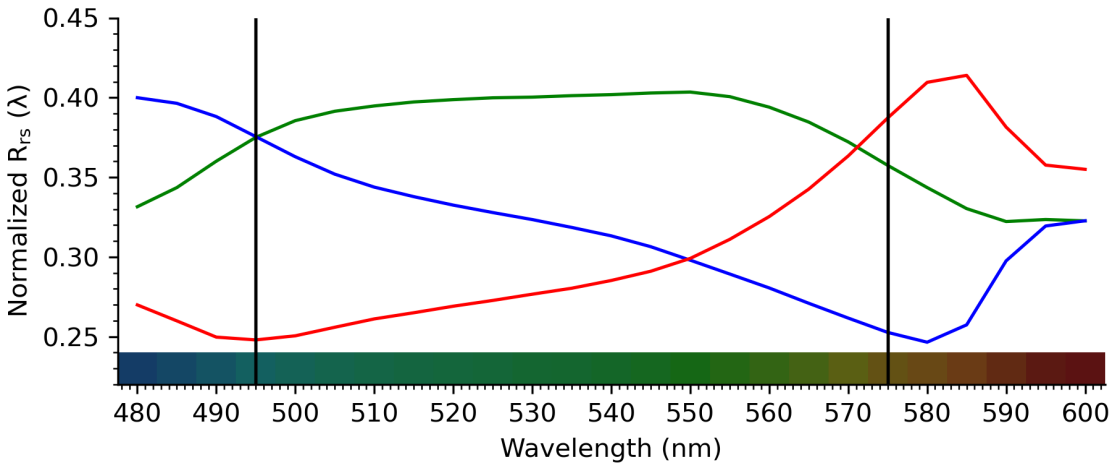

Figure S1: Normalized remote sensing reflectance spectra (R_{rs}) from 480 to 600 nm for three representative color types: blue (blue line), green (green line), and red/brown (red line) reservoirs. The reflectance was normalized to the total area under the curve. Vertical black lines mark the threshold wavelengths of 495 nm and 575 nm, used to delineate broad water color groups defined as blue ($\lambda_d \leq 495$ nm), green ($495 \text{ nm} < \lambda_d < 575$ nm), and brown ($\lambda_d \geq 575$ nm). The color gradient bar represents the perceived color based on Forel-Ule Index (FIU) color scale, illustrating the hue associated with each wavelength.

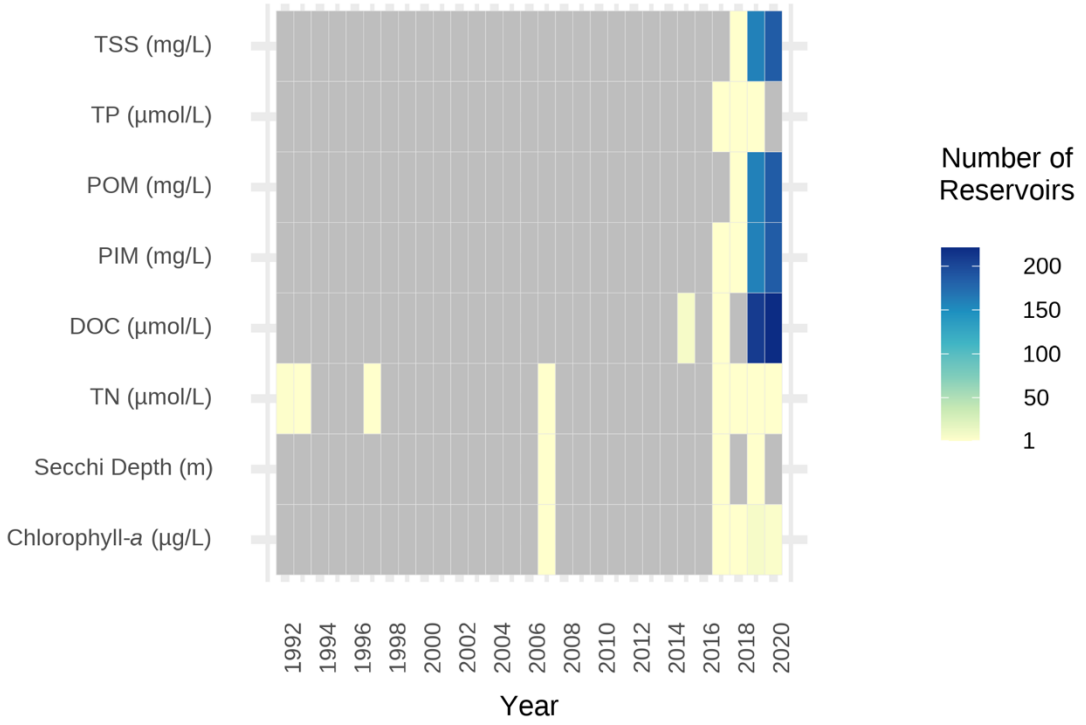

Figure S2: Number of epilimnetic samples used per variable and year when surface samples were not available.

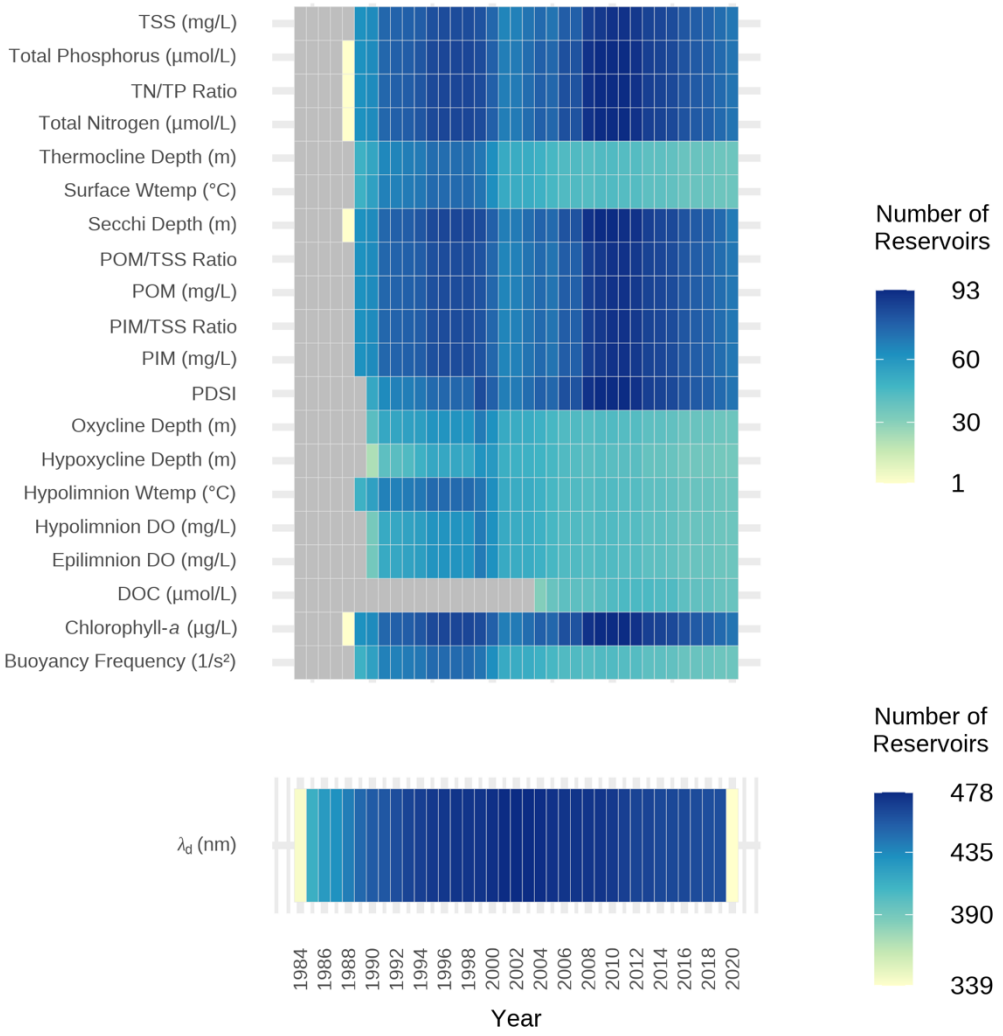

Figure S3: Number of reservoirs per variable and year included in the trend analysis. For dominant wavelength (λ_d), only reservoirs with a minimum of 20 consecutive years of data between 1984 and 2020 were included. For physical and chemical parameters, the analysis was limited to reservoirs with at least 10 consecutive years within the same period. Gray cells represent missing data.

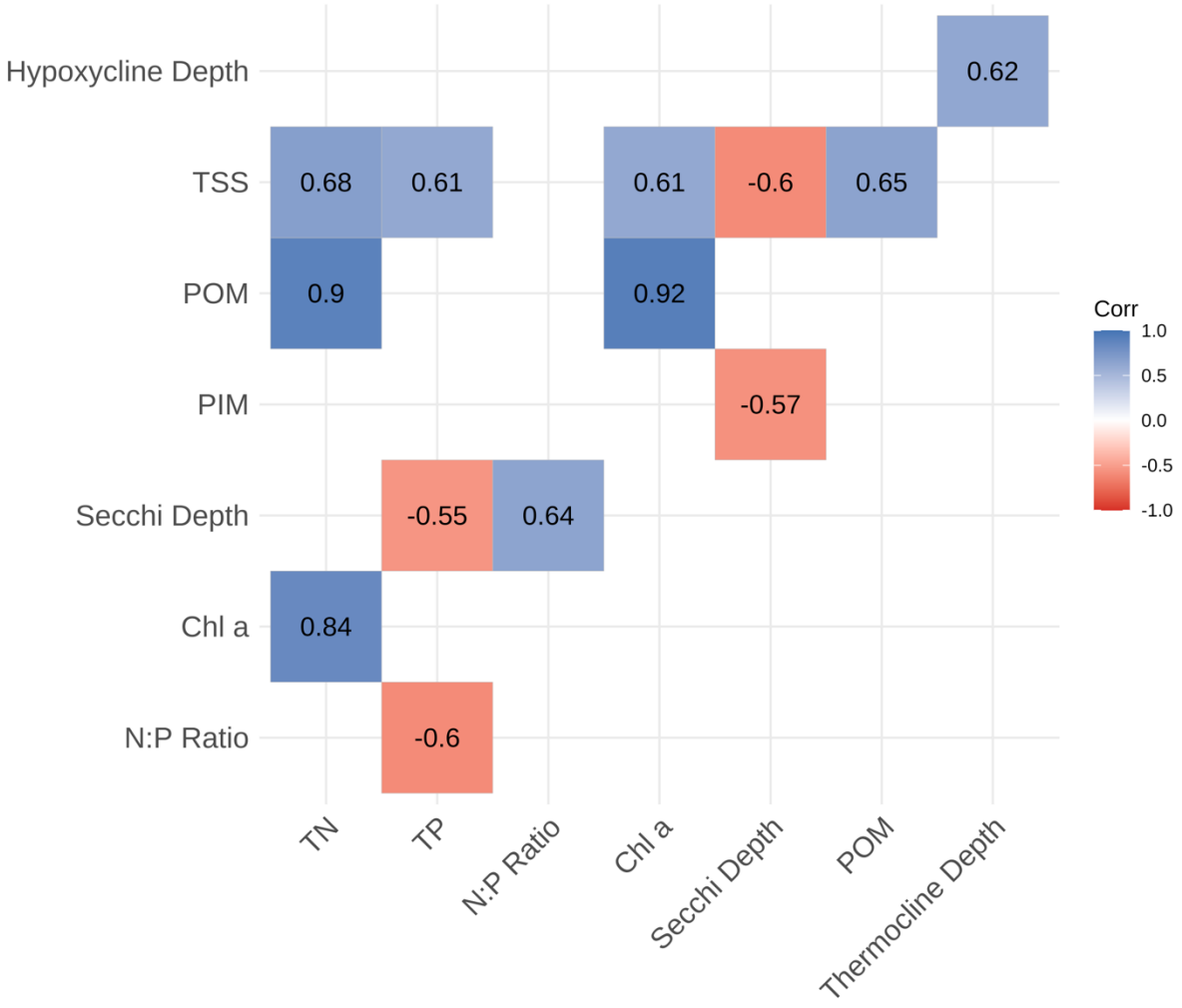

Figure S4: Spearman correlation matrix of water quality trends (i.e., slopes). Positive correlations are shown in blue and negative correlations in red. Only statistically significant correlations ($p \leq 0.05$) are displayed.

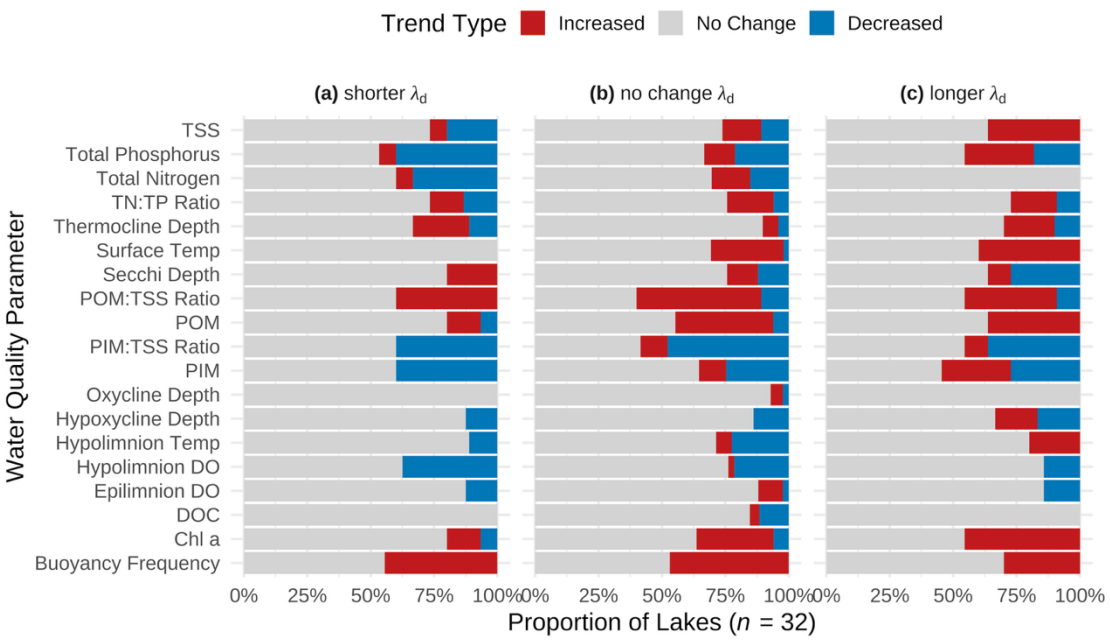

Figure S5: Proportion of lakes exhibiting increasing (red), no change (gray), or decreasing (blue) trends for multiple water quality parameters, grouped by the direction of dominant wavelength (λ_d) trends: (**a**) longer λ_d, (**b**) no change in λ_d, and (**c**) shorter λ_d. Results are based on 32 reservoirs with coincidental trends between λ_d and water quality parameters. Increased and decreased trends are statistically significant ($p \leq 0.05$).

References

Bartos, M., 2020. pysheds: Simple and fast watershed delineation in python. GitHub repository. https://github.com/mdbartos/pysheds.

Bartoń K (2024). MuMIn: Multi-Model Inference. R package version 1.48.4. https://CRAN.R-project.org/package=MuMIn.

Bates, D., Mächler, M., Bolker, B., Walker, S., 2015. Fitting linear mixed-effects models using lme4. J Stat Softw 67, 1–48.

Gillies, S., van der Wel, C., Van den Bossche, J., Taves, M.W., Arnott, J., Ward, B.C., et al., 2022. Shapely, Version 2.0.0. GitHub repository. https://github.com/shapely/shapely.

Greenwell, B., Boehmke, B., Cunningham, J., GBM Developers, 2022. gbm: Generalized Boosted Regression Models. R package version 2.1.8. https://CRAN.R-project.org/package=gbm.

Harris, C.R., Millman, K.J., van der Walt, S.J., Gommers, R., Virtanen, P., Cournapeau, D., Wieser, E., Taylor, J., Berg, S., Smith, N.J., Kern, R., Picus, M., Hoyer, S., van Kerkwijk, M.H., Brett, M., Haldane, A., del Río, J.F., Wiebe, M., Peterson, P., Gérard-Marchant, P., Sheppard, K., Reddy, T., Weckesser, W., Abbasi, H., Gohlke, C., Oliphant, T.E., 2020. Array programming with NumPy. Nature 585, 357–362.

Hijmans, R.J., Phillips, S., Leathwick, J., Elith, J., 2023. dismo: Species distribution modeling. R package version 1.3-15. https://CRAN.R-project.org/package=dismo.

Jones, J.R., Argerich, A., Obrecht, D. V, Thorpe, A.P., North, R.L., 2024a. Missouri lakes and reservoirs long-term limnological dataset, 1976-2018. Ver 2. Environmental Data Initiative (Accessed 2024-06-14).

Jones, J.R., North, R.L., Argerich, A., Thorpe, A.P., Obrecht, D. V, Price, A., Santamaria, K., Richardson, D.C., 2024b. Missouri reservoir profile data including temperature, depth, and oxygen profiles (1989-2022). Ver 2. Environmental Data Initiative (Accessed 2024-11-01).

Kendall, M.G., 1975. Rank Correlation Methods , 4th ed. Charles Griffin, London.

Kuznetsova, A., Brockhoff, P.B., Christensen, R.H.B., 2017. lmerTest package: Tests in linear mixed effects models. J Stat Softw 82, 1–26.

Laird, N.M., Ware, J.H., 1982. Random-Effects Models for Longitudinal Data. Biometrics 38, 963–974.

Lüdecke, D., Ben-Shachar, M., Patil, I., Makowski, D., 2020. Extracting, computing and exploring the parameters of statistical models using R. J Open Source Softw 5, 2445.

Mann, H.B., 1945. Nonparametric Tests Against Trend. Econometrica 13, 245–259.

Molnar, C., Bischl, B., Casalicchio, G., 2018. iml: An R package for interpretable machine learning. J Open Source Softw 3, 786.

North, R.L., Argerich, A., Obrecht, D. V, Thorpe, A.P., Richardson, D.C., 2025. Missouri reservoir water quality data from the Statewide Lake Assessment Program (SLAP), the Lakes of Missouri Volunteer Program (LMVP), and the Reservoir Observer Student Scientists (ROSS) program. Ver 1. Environmental Data Initiative (Accessed 2025-04-24).

Pohlert, T., 2020. trend: Non-parametric trend tests and change-point detection (R package version 1.1.4). https://CRAN.R-project.org/package=trend

Sen, P.K., 1968. Estimates of the regression coefficient based on Kendall's Tau. J Am Stat Assoc 63, 1379–1389.

Van den Bossche, J., Jordahl, K., Fleischmann, M., Richards, M., McBride, J., Wasserman, J., Badaracco, A.G., Snow, A.D., Ward, B., Tratner, J., Gerard, J., Perry, M., ..., Gardiner, J., 2024. geopandas/geopandas: Version 1.0.1. Zenodo.

Winslow, L., Read, J., Woolway, R., Brentrup, J., Leach, T., Zwart, J., Albers, S., Collinge, D., 2019. RLakeAnalyzer: An R package for analyzing lake data. Journal of R Package Development 10, 1–15.